

**REPORT DOCUMENTATION PAGE**Form Approved  
OMB NO. 0704-0188

Public Reporting burden for this collection of information is estimated to average 1 hour per response, including the time for reviewing instructions, searching existing data sources, gathering and maintaining the data needed, and completing and reviewing the collection of information. Send comment regarding this burden estimates or any other aspect of this collection of information, including suggestions for reducing this burden, to Washington Headquarters Services, Directorate for information Operations and Reports, 1215 Jefferson Davis Highway, Suite 1204, Arlington, VA 22202-4302, and to the Office of Management and Budget, Paperwork Reduction Project (0704-0188,) Washington, DC 20503.

1. AGENCY USE ONLY ( Leave Blank)		2. REPORT DATE 08/10/2004	3. REPORT TYPE AND DATES COVERED Final Report 05/01/01-06/30/04	
4. TITLE AND SUBTITLE Compound Semiconductor Based Two-Dimensional Photonic Crystal Light Sources			5. FUNDING NUMBERS DAAD19-01-1-0527	
6. AUTHOR(S) Pallab Bhattacharya				
7. PERFORMING ORGANIZATION NAME(S) AND ADDRESS(ES) Solid State Electronics Laboratory Department of Electrical Engineering and Computer Science University of Michigan Ann Arbor, MI 48109-2122			8. PERFORMING ORGANIZATION REPORT NUMBER	
9. SPONSORING / MONITORING AGENCY NAME(S) AND ADDRESS(ES) U. S. Army Research Office P.O. Box 12211 Research Triangle Park, NC 27709-2211			10. SPONSORING / MONITORING AGENCY REPORT NUMBER 42190.11-PH	
11. SUPPLEMENTARY NOTES The views, opinions and/or findings contained in this report are those of the author(s) and should not be construed as an official Department of the Army position, policy or decision, unless so designated by other documentation.				
12 a. DISTRIBUTION / AVAILABILITY STATEMENT Approved for public release; distribution unlimited.			12 b. DISTRIBUTION CODE	
13. ABSTRACT (Maximum 200 words) Two-dimensional photonic crystals (PC) have emerged as promising building blocks for integrated optics systems. Photonic crystal devices exploit defects, in an otherwise periodic lattice designed to exhibit a wide photonic bandgap (PBG), to form resonant microcavities or optical waveguides. The property of PC microcavities to enhance the source radiation into a desired mode while inhibiting other modes is particularly appealing for development of ultra-low threshold, single-mode lasers. In this final report we describe our work on the realization of photonic crystal vertically emitting microcavity light sources with electrical injection; edge emitting light sources integrated with PC-based waveguides; and PC-based resonant cavity photodiodes. We have realized the devices with GaAs- and InP-based QW and QD heterostructures. We also present a theoretical investigation of the spontaneous emission characteristics of an ensemble of self-organized InAs/GaAs QDs enclosed in the PC microcavity using guided modes as desired cavity modes. Combined with the molecular beam epitaxy and technology of self-organized QDs, photonic crystals can be further utilized to study single-dot lasing or for the observation of cavity electrodynamics (CQED) phenomena in semiconductor systems.				
14. SUBJECT TERMS			15. NUMBER OF PAGES 31	
			16. PRICE CODE	
17. SECURITY CLASSIFICATION OR REPORT UNCLASSIFIED	18. SECURITY CLASSIFICATION ON THIS PAGE UNCLASSIFIED	19. SECURITY CLASSIFICATION OF ABSTRACT UNCLASSIFIED	20. LIMITATION OF ABSTRACT UL	

NSN 7540-01-280-5500

Standard Form 298 (Rev.2-89)  
Prescribed by ANSI Std. Z39-18  
298-102

## **Final Progress Report**

- 1. Title of Project:** “Compound Semiconductor Based Two-Dimensional Photonic Crystal Light Emitters”
- 2. Grant Number:** DAAD 19-01-1-0527
- 3. Period Covered by Report:** 05/01/2001-06/30/2004
- 4. Name of Institution:** University of Michigan
- 5. Principal Investigator:** Pallab Bhattacharya  
**Co-principal Investigator:** Arthur McGurn
- 6. Scientific Progress and Accomplishments**

### **I. Introduction**

Two-dimensional photonic crystals (PC) have emerged as important basic structures for the realization of a new class of optical waveguides, filters, optical interconnects, lasers and detectors for in-plane integrated optics. Combined with the epitaxy and technology of self-organized quantum dots, PC can be utilized to study single-dot lasing or for the observation of cavity electrodynamics (CQED) phenomena in semiconductor systems. Photonic crystal devices exploit defects, in an otherwise periodic lattice designed to exhibit a wide photonic bandgap (PBG), to form microcavities or optical guides. If the material constituting the PC is photoluminescent, then a defect microcavity light source can be designed, provided that the luminescence spectrum overlaps the defect mode in the photonic bandgap. The property of PC microcavities to enhance the source radiation into a desired mode while inhibiting other modes is particularly appealing for development of ultra-low threshold, single-mode lasers. It is now well known that spontaneous emission is not an intrinsic atomic property. It can be modified by tailoring the electromagnetic environment that the atom can radiate into. In a single missing defect microcavity all photons corresponding to the wavelength of the defect, generated by recombination in the PBG crystal or otherwise, will be funneled into the single resonant mode of the defect and this mode can leak out of the crystal vertically or couple to an adjacent waveguide horizontally. Much progress has been made in the realization of planar two dimensional (2D) PC sources and waveguides but serious technological hurdles remain. For the PC emitters to be widely applicable, the issues of electrical injection and surface carrier recombination must be addressed in addition to the fabrication tolerances and the cavity quality factor.

In what follows, we summarize our work on the realization of quantum dot (QD) and quantum well (QW) photonic crystal microcavity light sources with electrical injection and devices integrated with PC-based waveguides. The devices are realized with GaAs- and InP-based QW and QD heterostructures.

## II. Electrically injected 0.94 $\mu\text{m}$ GaAs-based microcavity light source

### Summary

The characteristics of a GaAs-based single defect PC electroluminescent surface-emitting device are described. The single defect in a 2D PC, based on semiconductor heterostructures containing  $\text{In}_{0.15}\text{Ga}_{0.85}\text{As}$ –GaAs QWs, forms the microcavity. The light-current (L-I) characteristics are very different from conventional lasers, or even microcavity VCSELs. Data from the device indicate that light emission occurs from the microcavity formed by the defect and not from the rest of the 2D PBG. The device is, at best, a “few mode” LED. The concept of a threshold current, therefore, cannot be strictly applied, and instead, we see a gradual turn-on. We have analyzed this by the appropriate carrier and photon rate equations and by taking into account the substantial nonradiative recombination at the air holes.

### Design of PBG Crystal and Microcavity

The device heterostructure, grown by metal-organic vapor phase epitaxy (MOVPE), is shown in Fig. 2.1. It consists of an undoped cavity region of thickness with two  $70\text{\AA}$  pseudomorphic  $\text{In}_{0.15}\text{Ga}_{0.85}\text{As}$  QWs in the middle and p-type  $\text{Al}_{0.3}\text{Ga}_{0.7}\text{As}$  and contact layers on the top. N- and p-type  $\text{Al}_{0.96}\text{Ga}_{0.04}\text{As}$  layers are inserted for lateral wet-oxidation during the processing of the device. Therefore, the heterostructure is similar to that of an oxide confined VCSEL, without the top distributed Bragg reflector (DBR) mirror. The reflectivity of the top surface is that provided by the semiconductor-air

GaAs	0.0574 $\mu\text{m}$	p	$3 \times 10^{18}$
$\text{Al}_{0.8}\text{Ga}_{0.2}\text{As}$	0.0863 $\mu\text{m}$	p	$3 \times 10^{18}$
GaAs	0.0574 $\mu\text{m}$	p	$3 \times 10^{18}$
$\text{Al}_{0.96}\text{Ga}_{0.04}\text{As}$	0.08815 $\mu\text{m}$	p	$3 \times 10^{18}$
$\text{Al}_{0.3}\text{Ga}_{0.7}\text{As}$	0.1234 $\mu\text{m}$	p	$3 \times 10^{17}$
$\text{In}_{0.15}\text{Ga}_{0.85}\text{As}$	7 nm	i	-----
$\text{Al}_{0.3}\text{Ga}_{0.7}\text{As}$	8 nm	i	-----
$\text{In}_{0.15}\text{Ga}_{0.85}\text{As}$	7 nm	i	-----
$\text{Al}_{0.3}\text{Ga}_{0.7}\text{As}$	0.1234 $\mu\text{m}$	i	-----
$\text{Al}_{0.96}\text{Ga}_{0.04}\text{As}$	0.08815 $\mu\text{m}$	n	$2 \times 10^{18}$
GaAs	0.0574 $\mu\text{m}$	n	$2 \times 10^{18}$
$\text{Al}_{0.8}\text{Ga}_{0.2}\text{As}$	0.0863 $\mu\text{m}$	n	$2 \times 10^{18}$
n+ GaAs (100) substrate and buffer			

**Fig 2.1** (a) Device heterostructure grown by MOVPE on n+ GaAs substrate with two  $70\text{\AA}$   $\text{In}_{0.15}\text{Ga}_{0.85}\text{As}$  quantum wells in a  $\lambda$ -cavity.

interface. The bottom DBR was incorporated to achieve a high index step (reflectivity) in the bottom side and to ensure leakage of light from the top surface.

The cavity was designed with a 2-D PBG encompassing the peak emission wavelength at a normalized frequency of  $a/\lambda$  for the TE modes. In our case, the PBG center frequency  $a/\lambda=0.426$ , which corresponds to the quantum-well peak emission

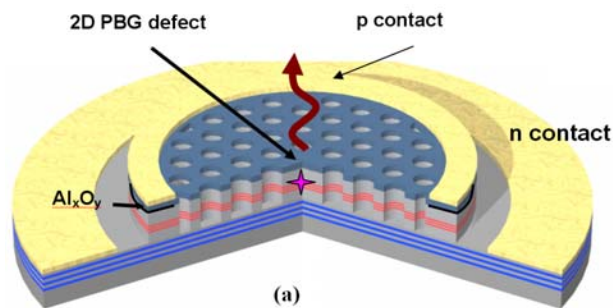
wavelength of 0.94  $\mu\text{m}$ . Values of  $a$  and  $r$ , 0.4 and 0.13  $\mu\text{m}$ , respectively, give the best experimental results, and we believe these dimensions place the QW emission within the PBG of the 2D crystal. Some amount of trial and error was involved since only a quasi-3D model was used.

### Device Fabrication

Mesa-etched devices with p- and n-contacts were first fabricated by optical lithography, dry and wet etching, metallization, and polyimide planarization. Lateral wet-oxidation of the  $\text{Al}_{0.96}\text{Ga}_{0.04}\text{As}$  layers was used here to funnel the charge carriers more efficiently into the center of the PBG region, which is next formed by electron beam lithography, pattern transfer, and deep dry etching techniques. The window inside the oxide ring is measured to be  $\sim 40 \mu\text{m}$  in diameter. A single defect in the center defines the  $\lambda$ -sized microcavity. The 0.8  $\mu\text{m}$  deep etch goes through the entire cavity region and well into the bottom DBR to ensure a good overlap with the optical field.

A schematic of the complete device with p- and n-type contact metallizations is shown in Fig. 2.2(a), together with scanning electron microscope (SEM) images of the PBG and the defect [Fig. 2.2(b) and (c)]. The active area aperture, created by the single defect, is surrounded by over 40 periods of PBG, having an extent (radius) of 20  $\mu\text{m}$ , which also coincides with the current funneling aperture formed by wet oxidation of the  $\text{Al}_{0.96}\text{Ga}_{0.04}\text{As}$  layers. Excellent diode characteristics were measured for the device at various stages. The reverse leakage current increased from 40 pA to 1 nA after formation of the PBG crystal.

Room-temperature photoluminescence (PL) measurements were also done on the as-grown heterostructures and on the samples after etching of air holes to form the PBG. The measurements were made with a 632-nm laser, 1-m scanning spectrometer, and a liquid-nitrogen cooled photomultiplier with lock-in amplification of the signal. This output is predominantly transverse-electric (TE) polarized due to the compressive strain in the InGaAs QWs. This is an advantage, since the PBG defect mode is predominantly TE polarized. It may also be noted that the peak intensity (940 nm) of the PL signal from the PBG region is at least ten times lower than that from the as-grown heterostructure. We also fabricated oxide-confined microcavity VCSEL-like devices with the epitaxial heterostructures before etching the air holes. No top DBR mirror was formed. These devices did not show lasing behavior. These control experiments are crucial in eliminating other possible sources of light emission that is subsequently observed in the devices with the PBG crystal with single defect.



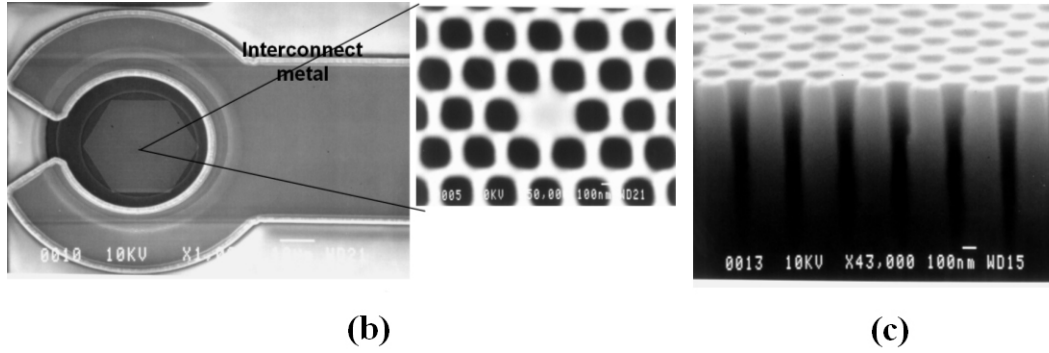


**Fig. 2.2** (a) Schematic of the electrically injected PC surface-emitting light emitter with single defect forming the microcavity. (b) SEM images of top view of a fabricated device with top electrical ohmic contact surrounding the PBG with the single defect magnified in the inset. (c) Cross-sectional SEM image of the 2D PBG slab.

### Device Characterization

The L-I and spectral characteristics of the PBG microcavity devices were measured in the pulsed mode (1 $\mu$ s width with 1% duty cycle) with probe contacts. The output was measured in a direction normal to the surface. It may be remembered that the dominant mode in the defect region can propagate laterally, or leak out vertically. The DBR mirror at the bottom helps in surface emission from the top. A turn-on, or soft threshold-like behavior in the injection current is consistently observed in the L-I characteristics (Fig. 2.3).

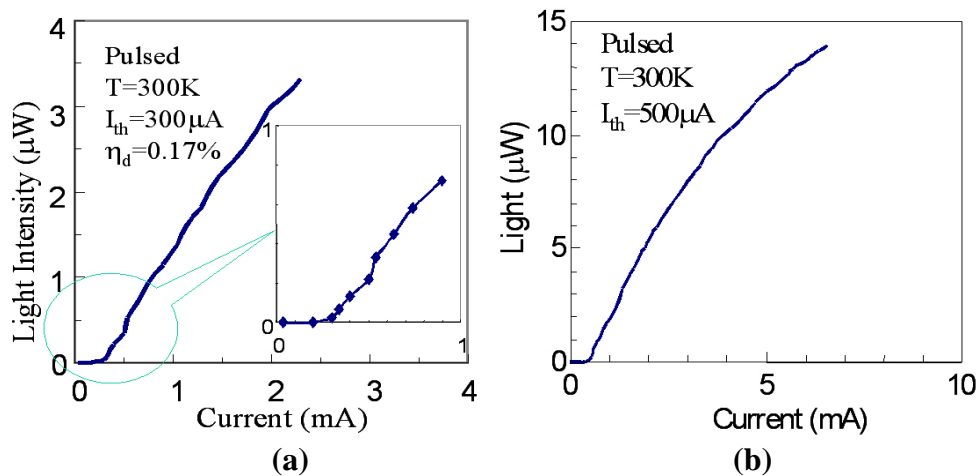


**Fig. 2.3** L-I characteristics of the single-defect PBG device at 300K in pulsed mode showing: (a) “soft” threshold current of 300  $\mu$ A and (b) maximum power output of 14.4  $\mu$ W.

The maximum output power is 14.4  $\mu$ W [Fig. 2.3 (b)]. The measured spectral outputs at different injection currents, below and above the turn-on, or threshold, are shown in Fig. 2.4. The spectra at low injection currents, below the turn-on, are also characterized by several distinct peaks, rather than a broad output. From a lineshape analysis of the main peak at 931 nm (above threshold), we derive a linewidth of 8 $\text{\AA}$ , which leads to a quality factor Q ( $\lambda/\delta\lambda$ ) of  $\sim$ 1164. This is, of course, different from the cold cavity Q, which we believe is lower in value. Our spectral data are also very noisy due to low

output power, in addition to multimode behavior, thereby making the linewidth measurements less accurate. We estimate the Q value to be  $\sim 200$ . It may be noted that the vertical cavity Q is very low ( $\sim 12$  in our case) since there is no DBR on the top surface. The peak output wavelength corresponds to a normalized frequency of 0.43, which is within the bandgap of the PC incorporated in our device. While the PL emission peaks at 940 nm at 300 K, the output emission center wavelength is 931 nm. We believe the shift is mainly due to the process induced PBG position and defect level shift.

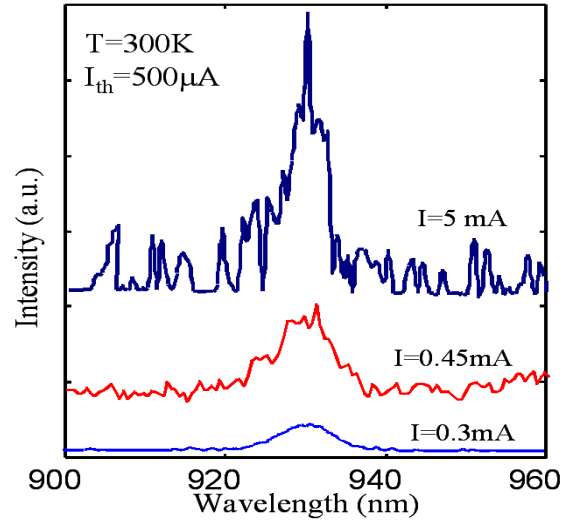


**Fig. 2.4** Measured spectral outputs for the device at different biasing currents. The peak emission for an injection current of 5mA is at 931nm with a linewidth of  $\sim 8\text{\AA}$ .

The field distribution and the localized defect mode in and around the defect in the PC were also calculated. The computations reveal that most of the energy of the defect mode leaks in the vertical (z) direction, rather than being guided in the plane (x-y) of the PC. The modes are predominantly TE, with a small contribution from unguided transverse magnetic (TM) modes. Fig.2.5 (a) shows the calculated dominant TE modes in the middle of the cavity for x and y dipole, respectively, which have a symmetrical distribution and extend radially through the first few periods of the air holes in the photonic crystal. The distribution is that of a pair of degenerate dipole modes, which may be present in the measured output spectrum of Fig. 2.4. We have also measured the near-field image [Fig. 2.5(b)] of the light output for an injection current of 2.2 mA, which is above threshold. It is evident that the modes spread out from the defect (microcavity) region during its propagation along the vertical direction. The nonuniformity in the mode profile is possibly due to light scattering in the air holes and diffraction at the surface. Nonetheless, it is important to note that the  $4\mu\text{m}$  lateral extent of the near field image is much smaller than the oxide window diameter of  $40\mu\text{m}$  and further helps to exclude the possibility that the entire 2-D-PBG crystal beyond the defect microcavity contributes to the observed output. Ideally, there should be a rapid decay of the electromagnetic fields inside the PBG lattice. In our case, the fact that the measured near-field image extends out to five lattice periods implies a spreading out of some sort, and the image may not exactly map the real field distribution pattern inside the cavity.

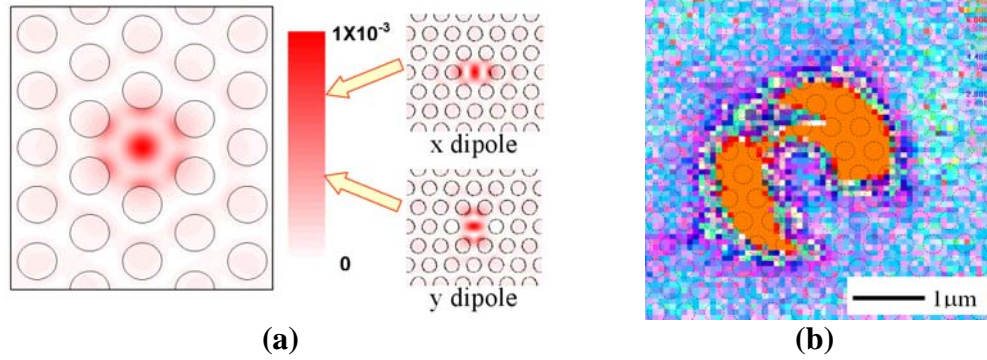


**Fig. 2.5** (a) Calculated electric field energy distribution (TE) in a horizontal (x-y plane) slice of the middle of the single-defect PBG crystal showing two degenerate modes localized in the single defect. (b) Measured near-field image of the device output on the 2-D air-hole PC pattern.

It may also be noted that the QW emission overlaps with the bottom of the air band at the M point, and this emission can, therefore, couple with the airband- guided modes propagating in the  $\Gamma\text{M}$  direction. The nearfield image indicates increased leakage in the  $\Gamma\text{M}$  direction. However, it cannot be confirmed whether only the dipole defect mode or a combination of defect and air-band modes are observed. Finally, we have also measured the far-field radiation pattern in devices with and without PBG crystal formation. The linewidth (full-width at half-maximum) of the pattern is  $\sim 30^\circ$ , in contrast to  $90^\circ$  for larger oxide-confined light-emitting diodes, confirming that the observed light output originates from the single-defect microcavity. The enhancement in spontaneous emission due to the microcavity effect (Purcell factor) was estimated from the measured cavity and a calculated effective modal volume  $V_{\text{eff}} \sim 3(\lambda/2n)^3$ . An enhancement by a factor of 15 is derived based on the calculated effective modal volume. The measured polarization characteristics of the device at an injection current of 4 mA is shown in Fig.2.6. Although a preferential polarization direction can be easily identified, output is clearly not in one definite polarization state, which is in agreement with data reported from a similar defect mode laser with optical pumping. We attribute the polarization behavior to the fact that the emission peak output consists of at least a pair of degenerate modes. By lowering the cavity symmetry, a single defect mode cavity can be formed and we expect a better-defined linearly polarized output.

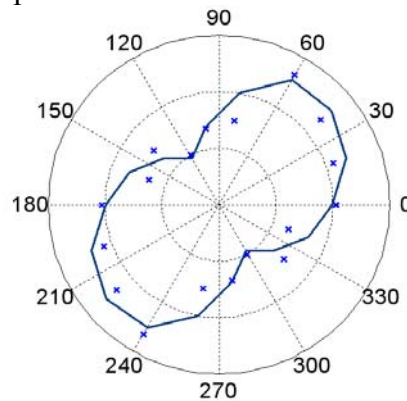


**Fig. 2.6** Measured polarization characteristics of the device (at  $\lambda=931$  nm) for an injection current of 4 mA. It is evident that the output does not display a single definite polarization.

It is also important to try and understand the nature of the light output and whether a true threshold can be expected. The injected carriers reach the defect (microcavity) by traveling around the air-hole columns in the PC. Some carriers may also travel via the top surface. This region, defined by the wet-oxidized AlGaAs layers, is 40  $\mu\text{m}$  in diameter. It can, therefore, be assumed that some fraction of the initial injection current is lost to nonradiative recombination, of which surface recombination is the dominant component. The surface recombination current can be expressed in terms of surface recombination velocity as

$$I_s = qS_0(np)^{1/2} L_s L_p \quad (1)$$

where

$(np)^{1/2}$  carrier density at the surface;  
 $L_s$  surface diffusion length;  
 $L_p$  perimeter length of the interface.

By taking  $S_0 = 10^6$  cm/s,  $L_s = 1$   $\mu\text{m}$  (total etch depth),  $L_p = 2\pi r$  with  $m$ , we get values of the surface recombination current through the holes and on the surface to be 96 and 14  $\mu\text{A}$ , respectively, adding to a total of 110  $\mu\text{A}$ . Since the observed soft threshold occurs at a larger value of injection current, it is believed that, for injection currents larger than 110  $\mu\text{A}$ , radiative recombination dominates.

It is also important and necessary to understand the nature of the L–I characteristics, especially at and near the “soft” threshold, or turn-on, region. For a true microcavity, the number of modes is limited to one, or a few, and the value of the spontaneous emission factor  $\beta$  is greatly enhanced. Theoretically, a microcavity light source formed by a single defect in a photonic crystal should have a near unity value of spontaneous emission factor  $\beta$ . We have analyzed the measured L-I characteristics with the rate equations for carriers and photons in microcavity lasers. The carrier density in the active region and the photon population  $P$  in the cavity can be described by the following rate equations:

$$\frac{dN}{dt} = \frac{I}{qV} - \frac{N}{\tau_{sp}} - \frac{N}{\tau_{nr}} - \Gamma \frac{gP}{V} \quad (2a)$$

$$\frac{dP}{dt} = \Gamma \frac{gP}{V} - \frac{P}{\tau_p} + \beta \frac{NV}{\tau_{sp}} \quad (2b)$$

where

$I$  injection current;  
 $q$  electron charge;  
 $V$  active region volume;  
 $\tau_{nr}$  nonradiative recombination lifetime;  
 $\tau_{sp}$  spontaneous emission lifetime;  
 $\tau_p$  stimulated emission lifetime;  
 $\Gamma$  confinement factor;  
 $g$  carrier density dependent gain.

$g$  can be expressed in terms of the transparent carrier density  $N_0$  and the differential gain as

$$g = \frac{dg}{dN} (N - N_0) = \frac{\beta V}{\tau_{sp}} (N - N_0) \quad (3)$$

It is also important and necessary to understand the nature of the L–I characteristics, especially at and near the “soft” threshold, or turn-on, region. For a true microcavity, the number of modes is limited to one, or a few, and the value of the

spontaneous emission factor  $\beta$  is greatly enhanced. Theoretically, a microcavity light source formed by a single defect in a photonic crystal should have a near unity value of spontaneous emission factor  $\beta$ . We have analyzed the measured L-I characteristics with the rate equations for carriers and photons in microcavity lasers. The steady-state solution of the rate equations yield the output L-I characteristics. As can be seen in Fig. 2.7, good agreement between measured and calculated data is obtained for  $\beta \sim 0.06$  by taking into account a relatively large nonradiative surface recombination induced carrier loss ( $\tau_{sp} \ll \tau_{nr}$ ) and photon scattering loss in the device. A photon lifetime of 1 ps and an optical confinement factor of 0.05 are used in the analysis. It may be noted that the value of  $\beta$ , although less than unity, is significantly larger than that in conventional semiconductor lasers ( $\beta \sim 10^{-4}-10^{-5}$ ).

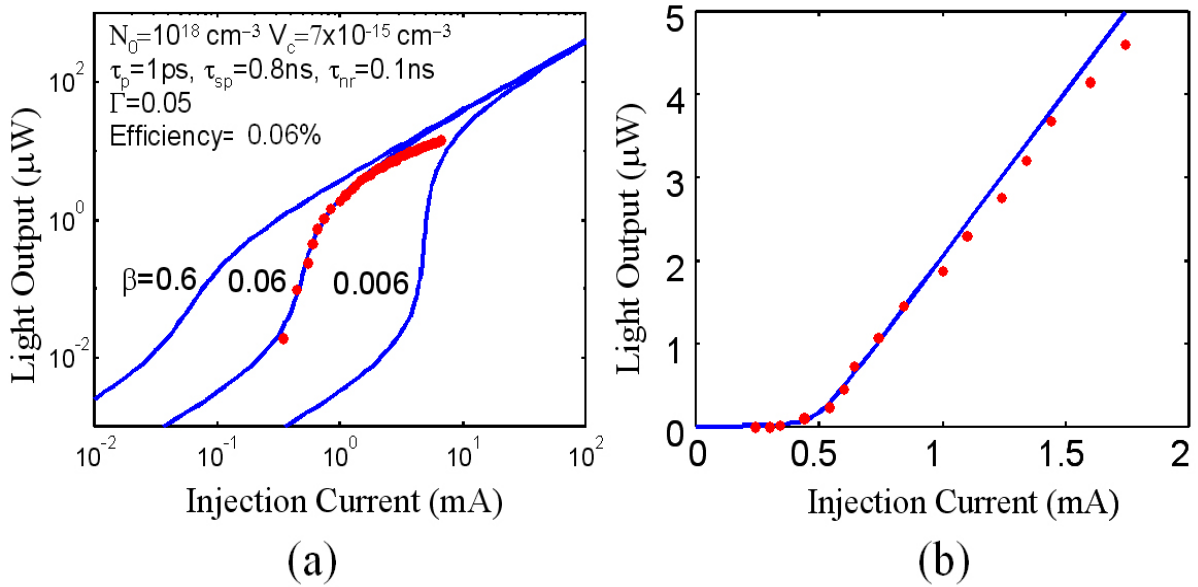


**Fig. 2.7** Numerical fit of the measured L-I characteristics (sold dots) to the calculated L-I characteristics for a microcavity light emitter (solid lines), showing good agreement for a spontaneous emission factor  $\beta=0.06$ , which indicates strong spontaneous emission control: (a) logarithmic and (b) linear scales.

### III. Electrically injected 1.55 $\mu\text{m}$ InP-based photonic crystal microcavity light source

#### Summary

An InP-based 1.55  $\mu\text{m}$  microcavity surface-emitting light source operating under pulsed current injection at room temperature has been designed and fabricated. The microcavity is formed by single or multiple defects in the center of a 2D PC consisting of an InP-based heterostructure. The gain region consists of 9 80 $\text{\AA}$   $\text{In}_{0.584}\text{Ga}_{0.416}\text{As}_{0.898}\text{P}_{0.102}$  pseudomorphic QWs that exhibit a spontaneous emission peak at 1.55 $\mu\text{m}$ . The light-current characteristics of the device exhibit a gradual turn-on, or a soft threshold, typical of single- or few-mode microcavity devices at 1mA.

## Fabrication and Design

The InP-based laser heterostructure is grown by MOCVD. It consists of an n+ InP contact layer, an n-type bottom InP/InGaAsP distributed DBR mirror, an undoped 1.55 $\mu\text{m}$   $\lambda$ -cavity with 9 80 $\text{\AA}$   $\text{In}_{0.584}\text{Ga}_{0.416}\text{As}_{0.898}\text{P}_{0.102}$  pseudomorphic QWs in the middle and p-type InGaAsP and contact layers on the top. A p-type AlInAs layer are also inserted on top of the cavity region for eventual lateral wet-oxidation during the processing of the device. Figure 3.1(a) shows the device heterostructure. The photoluminescence emission peak from the QWs is observed at 1.55  $\mu\text{m}$ . Standard oxide-confined VCSEL process steps were used in the device fabrication with a combination of optical lithography, dry and wet etching, metallization and polyimide planarization. The 2D PC formation is achieved afterwards using the Leica/Cambridge EBMF ebeam lithography tool, a metal-on-polyimide process to reverse the ebeam pattern followed by anisotropic high temperature dry etching of the pattern into the InP heterostructure using a PlasmaQuest ECR source. The deep etch goes through the entire cavity region. A single or multiple defects in the center define the lambda-sized microcavity, which was designed with the PBG encompassing the peak emission wavelength of 1.55 $\mu\text{m}$ .

The cross-section of the 2D PC is shown in Fig. 3.1. The active area aperture, created by the single defect is 0.8 $\mu\text{m}$ . This aperture is surrounded by 65 periods of the PC, having an extent (radius) of 30  $\mu\text{m}$ .

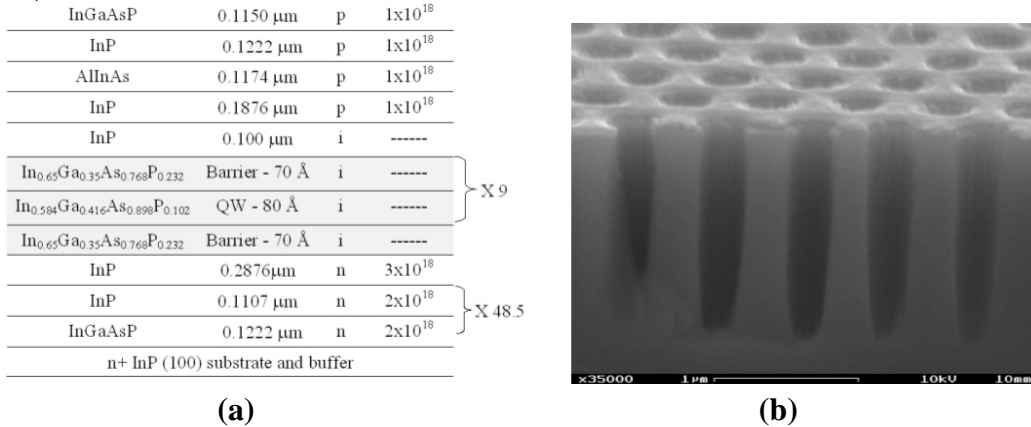


**Fig 3.1** (a) Device heterostructure grown by MOCVD on n+ InP substrate with 9 80 $\text{\AA}$   $\text{In}_{0.584}\text{Ga}_{0.416}\text{As}_{0.898}\text{P}_{0.102}$  quantum wells in a  $\lambda$ -cavity; (b) Cross Section SEM of InP photonic crystal after ebeam patterning, pattern reversal and deep etch with the PlasmaQuest ECR source.

## Device Characteristics

Light-current characteristics of the InP devices were measured in pulsed mode before and after the formation of the photonic crystal defect. Fig. 3.2 shows the L-I measured from a device without the PC (which is basically a VCSEL cavity without the top DBR) which shows typical LED characteristics. Fig. 3.3(a) shows the L-I with a single period defect cavity at the center of the photonic crystal with the “soft” threshold behavior at  $I=1\text{mA}$ . Fig. 3.5(b) shows the L-I characteristics of 1 and 3 defect period cavities. We find that slope efficiency increases by a factor of 22 with decrease in size of the cavity. A steady state rate equation analysis reveals that the fitted spontaneous emission parameter,  $\beta=0.01$ , while in conventional lasers,  $\beta$  is about  $10^{-4}$ - $10^{-5}$ .

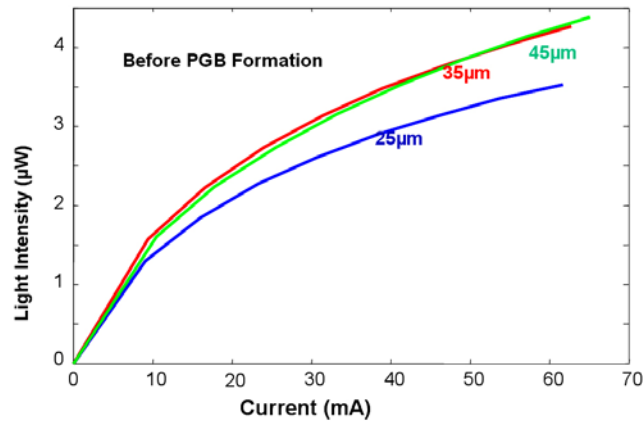


**Fig. 3.2** Room temperature light current characteristics of 1.55 μm surface emitting device before photonic crystal formation (i.e. VCSEL without top DBR) for different oxide apertures.

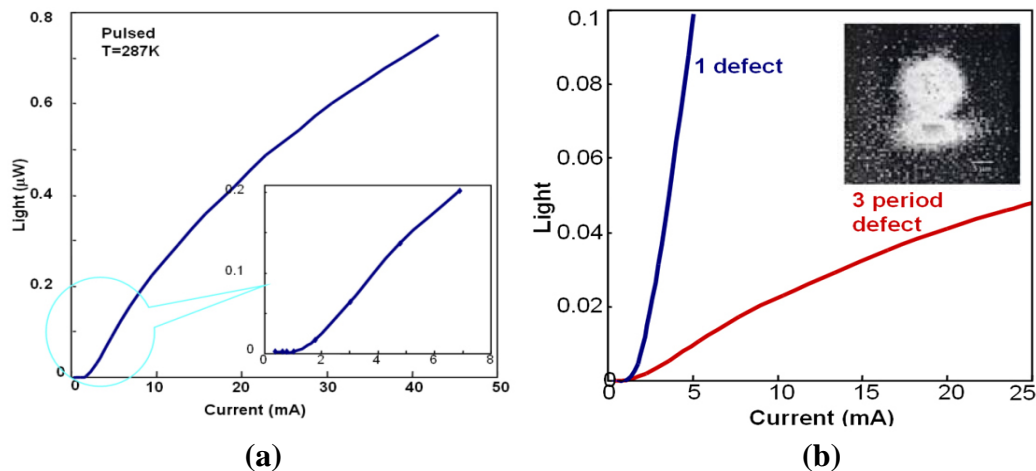


**Fig. 3.3** (a) L-I (pulsed mode) characteristics (a) single defect microcavity with aperture size is  $\sim 0.8 \mu\text{m}$  and “soft” threshold at  $I=1\text{mA}$ . (b) Comparison of L-I of 1 and 3 period defect apertures at the center of PBG showing an increase in the slope efficiency by a factor of 22. The near-field image if a single missing defect cavity is shown in the inset.

## IV. Quantum Dot Photonic Crystal Microcavity Light Emitter

### Introduction

Recently, self-organized QDs grown by MBE or MOVPE have been proven to be the nanostructures which best approach the desired properties of QDs, and almost all groups actively pursuing QD device development are utilizing self-organized growth. The use of biaxial strain during epitaxy to produce self-assembled QD structures has now become a well-accepted approach and is widely used in III-V semiconductors and other material systems. Much progress has been made in the area of growth -- where the focus has been size control, and optical characterization -- where the goal has been their application to QD lasers and detectors. The motivation for our work is to take the PC defect microcavity laser one step further by using self-organized QDs in the active region instead of a QW active region as we have done so far. Similar to a photonic microcavity which provides

three-dimensional confinement for photons, a QD can be thought of as providing a three-dimensional nanocavity for the electron-wave functions. QDs have higher density of states, higher gain and lower spontaneous emission lifetimes. Self-organized QD lasers made with In(Ga)As/Al(Ga)As pseudomorphic heterostructures have demonstrated very low threshold currents. By combining the electrical confinement properties of quantum dots along with the photonic confinement of a single defect PBG microcavity we can potentially get ultralow threshold (lower than that compared to QW microcavity lasers) or even thresholdless lasers and high speed operation. The QD active region provides the following advantages: Carrier and photon confinement in the same region – diffusion effects minimized; narrow emission (homogeneously broadened) linewidth of QDs can match singularity in photon DOS to produce true single mode LED; negligible optical loss by active material in the surrounding when QD is put in the defect and large optical non-linearities.

Theoretical calculations have also shown us the spontaneous emission is enhanced significantly with the incorporation of QDs in PC cavity. Our motivation is to study the properties of an electrically injected PC microcavity with self-organized quantum QDs. Fabrication of this device will be similar to the devices described in Sections 2 and 3, with the only difference being that the active QW will be replaced by QDs. The device has been designed to emit at  $1.04\mu\text{m}$ .

### Device Fabrication

The design and fabrication of an electrically injected surface emitting photonic crystal microcavity with  $1.04\mu\text{m}$  InAs/GaAs quantum dot active region is described. The GaAs based device heterostructure is grown by MBE. It consists of an n-type lower GaAs/Al<sub>0.8</sub>Ga<sub>0.2</sub>As bottom DBR mirror, an undoped  $\lambda$  cavity ( $\lambda=1.04\mu\text{m}$ ) region with five layer InAs/GaAs QDs active region and p-type AlGaAs and contact layers on the top. Fig. 4.1 shows the MBE grown heterostructure design. The 2D PC formation is achieved by e-beam lithography, pattern transfer and deep dry etching techniques. A single or multiple defects in the center define the  $\lambda$ -sized microcavity which was designed with the PBG encompassing the peak emission wavelength of  $1.04\mu\text{m}$ . Fig. 4.2 shows SEMs of the finished devices.

	GaAs	0.0746 $\mu\text{m}$	p <sup>+</sup>	$2 \times 10^{19}$
	Al <sub>0.8</sub> Ga <sub>0.2</sub> As	0.0854 $\mu\text{m}$	p	$2 \times 10^{18}$
	GaAs	0.0746 $\mu\text{m}$	p	$2 \times 10^{18}$
	Al <sub>0.96</sub> Ga <sub>0.04</sub> As	0.0879 $\mu\text{m}$	p	$2 \times 10^{18}$
	GaAs	0.1396 $\mu\text{m}$	i	-----
	InGaAs dots	QD	i	-----
X4	GaAs barrier	20 Å	i	-----
	InGaAs dots	QD	i	-----
	GaAs Spacer	0.1396 $\mu\text{m}$	i	-----
X29	Al <sub>0.96</sub> Ga <sub>0.04</sub> As	0.0879 $\mu\text{m}$	n	$2 \times 10^{18}$
	GaAs	0.0746 $\mu\text{m}$	n	$2 \times 10^{18}$
	Al <sub>0.8</sub> Ga <sub>0.2</sub> As	0.0854 $\mu\text{m}$	n	$2 \times 10^{18}$
n <sup>+</sup> GaAs (100) substrate and buffer				

**Fig 4.1** (a) Device heterostructure grown by MBE with an n-type lower GaAs/Al<sub>0.8</sub>Ga<sub>0.2</sub>As bottom DBR mirror, an undoped  $\lambda$  cavity( $\lambda=1.04\mu\text{m}$ ) region with five layer InAs/GaAs QDs active region and p-type AlGaAs and contact layers on the top.

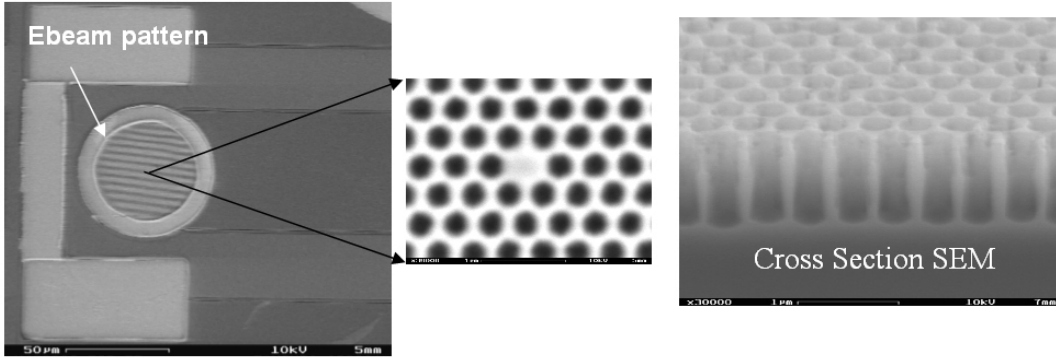


**Fig. 4.2** Schematic of a surface-emitting electrically injected device with QD active region and 2D PC horizontal confinement. The cavity is formed by a single defect in the 2D PBG.

### Device Characterization

We have examined the light-current characteristics of device fabricated as described above with a cavity defined by the photonic crystal defect. The L-I characteristics of 2- and 5-defect microcavity devices are presented in Fig. 4.3. The devices were tested on a Peltier cooler in pulsed-mode ( $1 \mu\text{s}$  with 1% duty cycle). A maximum light output of  $0.17 \mu\text{W}$  is measured from a single two-defect device, but the total output efficiency is extremely small,  $1.4 \times 10^{-3}\%$ . This could be due to various reasons, including the small recombination volume, defects in and around the dots, and imperfections in device processing, giving rise to surface recombination. It is also noticed in Fig. 4.3 that the output of the two-defect device is larger than that of the five-defect device. We have consistently recorded this trend in similar QW devices and we cautiously attribute it to microcavity effects.

The near-field image of the light output was also measured. The inset of Fig. 4.3 shows the output for an injection current of  $7.15 \text{ mA}$  injection.

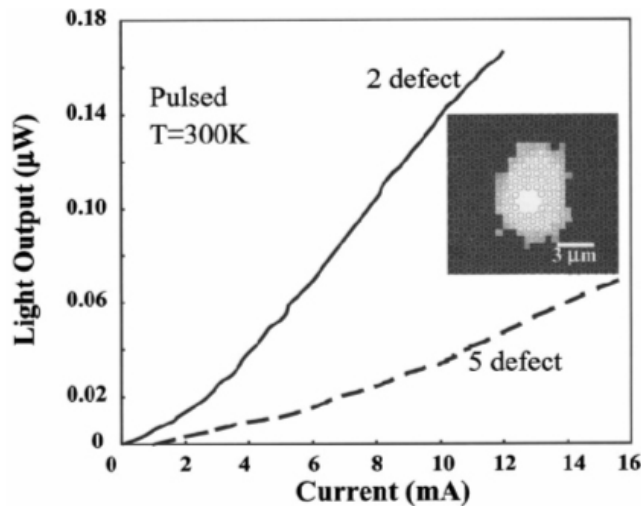


**Fig. 4.3** Light-current characteristics in pulsed-mode ( $1 \mu\text{s}$  with 1% duty cycle) of PC two- and five-defect period microcavity; inset shows the near-field image of two-defect period microcavity  $1.38 \text{ mm}$  surface diameter under  $7.15 \text{ mA}$  injection measured at a distance of  $4 \text{ mm}$  from the device surface.

It is important to note that even at this distance, where some amount of spreading takes place, the extent of the near-field image is several times smaller than the 50- $\mu\text{m}$ -diameter device aperture defined by wet oxidation of  $\text{Al}_{0.96}\text{Ga}_{0.04}\text{As}$ . There is also the possibility of light scattering in the air holes and diffraction at the surface. One has also to consider the possibility that we see light output from the central defect region because the patterned region is optically “darker” due to surface recombination. However, the injected holes from the top  $p$ -contact have to reach the active region by traversing around the etched holes. It is inconceivable that carriers traveling to the center defect region encounter fewer surface states than in traveling to the surrounding regions.

The PL of the annealed InAs/GaAs QDs, before fabrication of the PC and the rest of the device, was measured at 17 K using an Ar laser source, a monochromator, and liquid nitrogen cooled photomultiplier tube. Transitions represented by a peak and a shoulder are observed at 1.01 and 1.025  $\mu\text{m}$  with a separation of 20 meV, as shown in Fig. 4.4. We believe that these two peaks, respectively, correspond to transitions related to the excited and ground states of the QDs. After the device fabrication and formation of the photonic crystal, microPL measurements were performed using a 5 mW Ar laser source at 8 K. Figure 4.4 shows the measurements for a 5-defect cavity sample, and we notice two peaks, at 1.015 and 1.035  $\mu\text{m}$ , of almost equal intensity. Comparing with the as-grown PL we see that the stronger excited state transition of the sample before fabrication of the PC is suppressed while the weaker ground state transition is enhanced. This is likely due to the microcavity effect of the PC and the 1.035  $\mu\text{m}$  transition is in resonance with one of the dominant cavity modes.

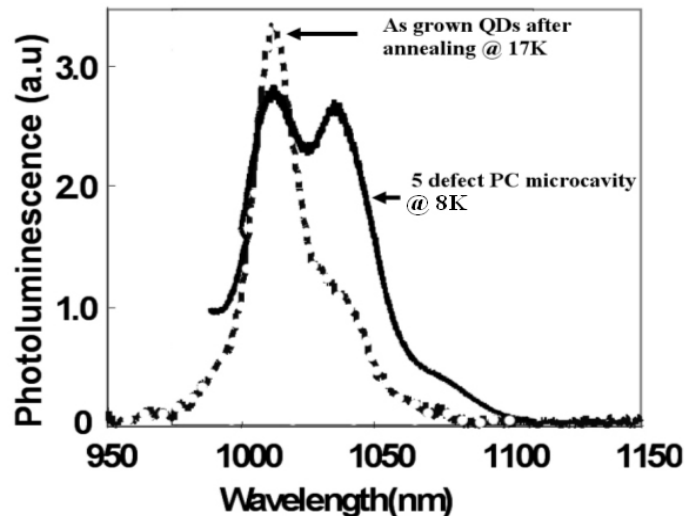


**Fig. 4.4** .PL of as-grown InAs/GaAs QDs at 17 K after annealing and micro-PL of QDs in a five-defect period photonic crystal microcavity at 8 K.

## V. Electrically Injected Photonic Crystal Edge Emitting Quantum Dot Light Source

### Summary

Electrically injected photonic crystal (PC) light sources with quantum dots (QDs) demonstrated in our group suffer from large non-radiative carrier surface recombination,

low injection efficiency, and the difficulty associated with integration with PC-based waveguides. We have successfully addressed these issues and fabricated a novel electrically injected 2D PC-based quantum dot edge emitting light source with coupled PC waveguide that avoids carrier recombination in PC air-holes and allows for easy integration with PC-based planar waveguides. The devices are based on a GaAs heterostructure with self-organized InGaAs QDs emitting at  $\sim 1\mu\text{m}$  and  $\sim 1.3\mu\text{m}$ . The emission spectra and near-field images indicate that the spontaneous emission from the low-Q resonant photonic crystal cavity is coupled to an adjacent photonic crystal missing defect waveguide and guided over the  $70\mu\text{m}$  waveguide length. The devices are easily integrable with planar PC-based waveguides and have a potential to become an important part of future integrated optoelectronic circuits.

### Device Design and Fabrication

One and three missing defect multimode waveguides were defined along the  $\Gamma$ -K direction and placed either alongside the cavity 2 lattice constants away from or pointing towards a vertex of the hexagon to couple the cavity modes with hexagonal symmetry and whispering-gallery-like modes transversely (Fig. 5.1(b)) or the linearly oscillating modes along  $\Gamma$ -K (Fig. 5.1(a)), respectively, generated in the cavity. Both single and three missing defect waveguides have been used in our devices.

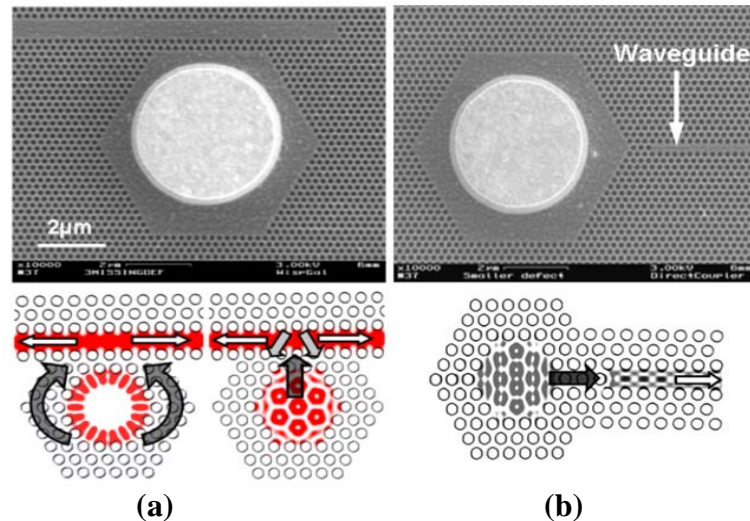


**Fig. 5.1** (a) A schematic of the mode coupling scheme in a device with a three-missing defect waveguide designed to couple  $\Gamma$ -K linearly resonant modes, (b) a schematic of a device with a single-missing defect waveguide designed to extract whispering-gallery-like modes (left) and resonant modes with hexagonal symmetry (right) transversely via anti-crossing mechanism. Coupling directions are indicated by arrows.

To understand the mode coupling in the cavity/waveguide devices it is necessary to investigate both the modes supported by the resonant cavity and the transmission spectra of the PC-based missing defect waveguides. Various cavities and waveguides were studied using a micro PL setup. Vertical PL spectra of a hexagonal cavity of 7 missing holes along a side of a hexagon (H7) with a W3 waveguide 2 periods away from the cavity is shown in Fig. 5.2. It is evident that the cavity supports numerous modes with  $Q\sim 600$  within the PBG of the crystal.

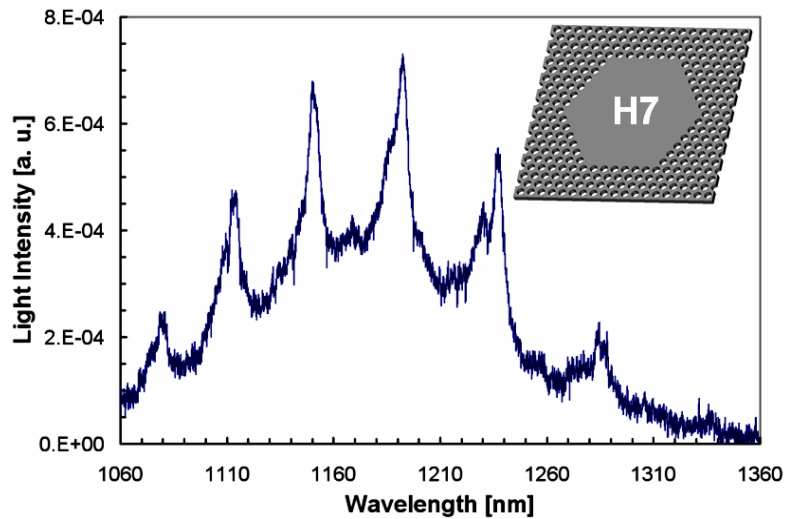


**Fig. 5.2** Measured resonant cavity modes supported by H7 PC cavity (shown in the inset).

Transmission through PC-based missing defect waveguides was studied using the same technique. A 10nm-wide mini-stopband was observed in the transmission spectra of W3 waveguides [Fig. 5.3]. The stop-band indicates the region of high mode coupling efficiency for devices in geometry shown in Fig. 5.1.

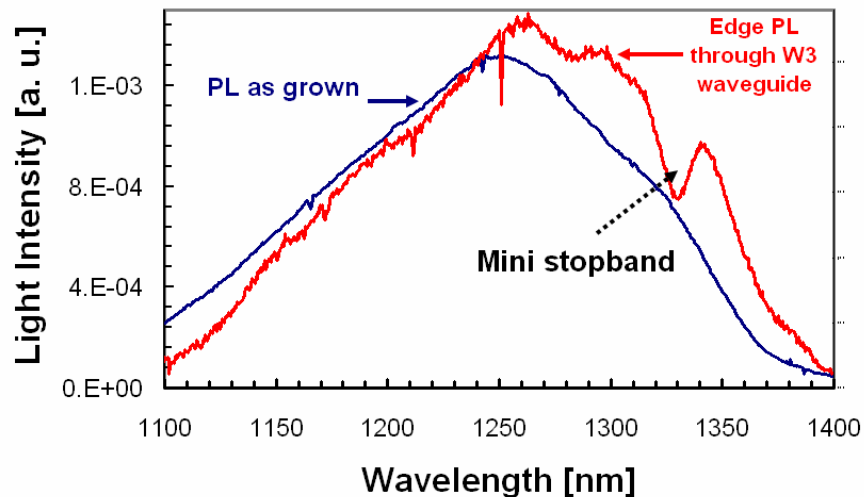


**Fig. 5.3** Measured edge PL spectra of the unpatterned QD heterostructure and a W3 missing defect PC-based waveguide.

Hexagonal cavities and waveguides are embedded in a triangular lattice of air holes in (001) GaAs-based epitaxially grown p-i-n heterostructures. The active light-emitting material consists of 4 coupled  $\text{In}_{0.4}\text{Ga}_{0.6}\text{As}$  quantum dot layers emitting at  $0.98\mu\text{m}$  with  $18\text{\AA}$  GaAs barrier layers buried in a  $0.21\mu\text{m}$  undoped GaAs layer. This is surrounded by  $1.05\mu\text{m}$   $\text{Al}_{0.3}\text{Ga}_{0.7}\text{As}$  layers on both sides. Both cavities and PC waveguides surrounded by 40 periods of bulk PC. In the final design the PC lattice constant is 240 nm and the hole diameter is  $\sim 150$  nm. The top p-metal contact was first defined by optical lithography and the upper  $\text{Al}_{0.3}\text{Ga}_{0.7}\text{As}$  cladding layer thickness around contact was

etched down to  $\sim 300$  nm. The PC pattern was defined with electron beam lithography and transferred to a silicon nitride mask used in the electron cyclotron resonance reactive ion etch (ECR-RIE). Photonic crystals with hole etch depths approaching 800nm, which are sufficient to penetrate the top cladding and the active region, were thus realized. A mesa surrounding the PC and the coupled waveguide was defined using photolithography to enable extraction of light from the end of the PC waveguide. The n-metal was then deposited on the n+ substrate forming a back-side contact. With the p-metal located directly above the resonant cavity and n-contact below it, the injected carriers recombine predominantly in the quantum dots and not in the PC surrounding the cavity. Non-radiative surface recombination in the PC air holes is thus minimized.

### Device Characterization

The devices were characterized at room temperature by light-current (L-I), near-field, and spectral measurements. The light generated in the PC microcavity and coupled to the PC waveguide was collected at the mesa etched facet. The L-I characteristics for transversely mode coupled devices with various cavity and waveguide sizes are illustrated in Fig. 5.4 (a).

It is observed that increasing cavity size and PC-based waveguide width lead to higher output power as the carrier recombination volume and number of possible couplings between cavity and waveguide modes increases. However, the maximum power is probably  $\leq 1$ nW. The moderate etch depth ( $\sim 800$ nm), hole morphology and presence of QDs in the waveguide increase the losses. Although the out-of-plane losses are high, the light is well confined horizontally by the PC waveguide as evidenced by the near-field image of the output spot size on the mesa facet, (inset of Fig. 5.4(a)). However, scattered light coming from outside the cavity was observed with lower magnification lenses. This suggest that not all of the light collected by the spectrometer is PBG guided. The device spectra are shown in Fig. 5.4(b). Two broad peaks correspond to the mode anti-crossing regions in the waveguide dispersion curves.

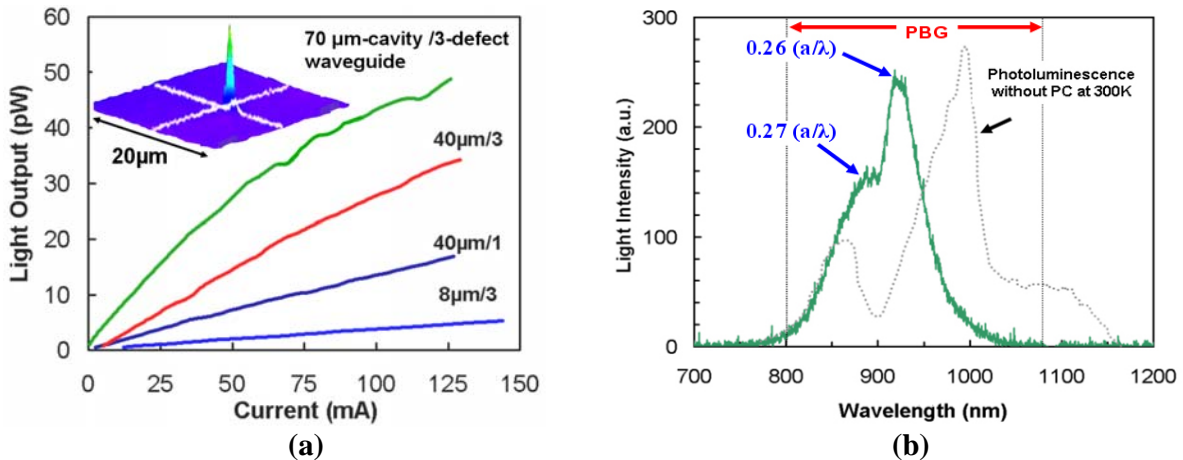


**Fig. 5.4** (a) Measured light-current characteristics for various cavity and waveguide sizes in the configuration shown in Fig. 1(a) at 300K. The 3D near-field image of the output spot is shown in the inset, and (b) the spectral characteristics.

The presence of QDs in the waveguide portion of the emitter described in the previous section presents a significant limitation to the device performance. Possible solutions to avoiding QD light re-absorption include introduction of twin-guide structures where the active region and guiding region are vertically separated (Fig. 5.5(a)).

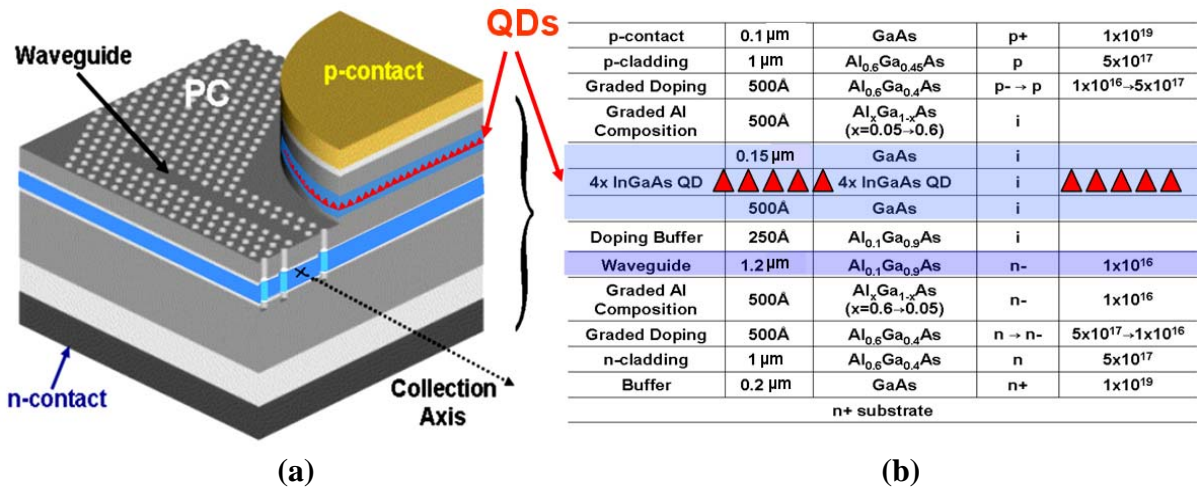


**Fig. 5.5** (a) Schematic of a twin-guide structure with the quantum dot active region vertically separated from the passive waveguide, and (b) twin-guide heterostructure.

Preliminary results are very promising as the total power output from these devices is considerably higher than from the previous devices. The emitted light is very well horizontally confined as shown in Fig. 5.6(a). The bright spot A is the light guided by the waveguide. Spectral characteristics of this light are dictated by the resonant cavity modes that are coupled to waveguide modes via anti-crossing mechanism and the spectral narrowing due to resonant cavity effects is observed (Fig. 5.6). This preliminary data was obtained with a low resolution spectrometer ( $<4\text{nm}$ ). The presence of light region B and C can be attributed to the scattered light not modulated by the PC resonant cavity.

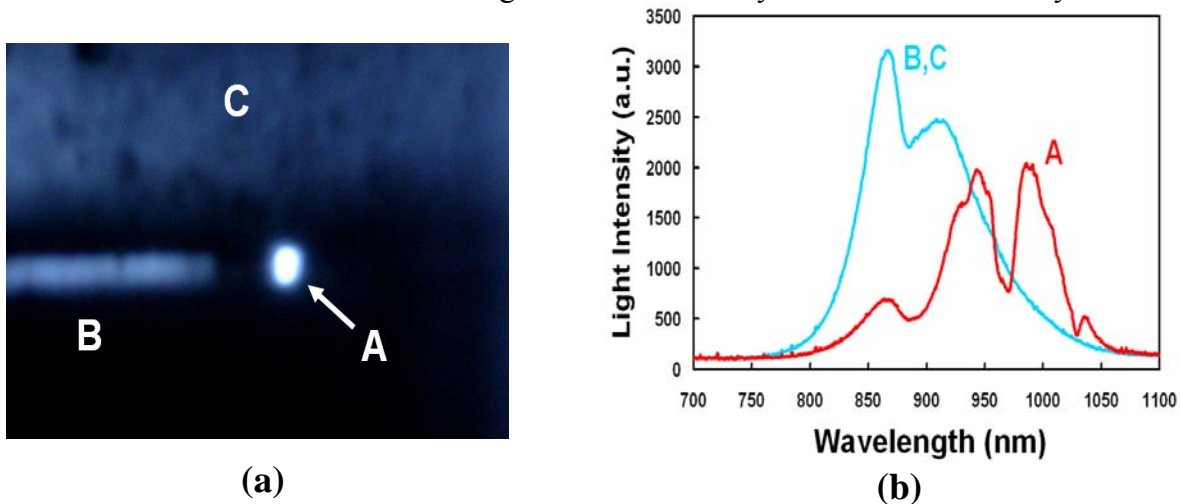


**Fig. 5.6** (a) Near-field image of the output spots of the device with the twin-guide heterostructure, and (b) spectral characteristics of the light coupled through the PC waveguide (A) and electroluminescence of the QD heterostructure (B and C).

The output spectra should reflect the properties of PC microcavities and waveguides. An important parameter that needs to be determined is the coupling efficiency between the PC resonant cavity modes and the PC-based missing defect waveguides. We have fabricated and characterized a quantum dot based photonic crystal PC light emitting diode, monolithically integrated with a transversely coupled PC waveguide. Two types of cavity-waveguide coupling have been considered. The emission spectra reveal that all anti-crossing couplings between cavity and waveguide are involved in the output coupling process.

The external quantum efficiency, given by the number of transmitted photons to that of injected carriers, is defined by three processes in a light emitting diode: the injection process, the recombination process, and the extraction process. These processes are quantified by their respective efficiencies: the injection efficiency,  $\eta_{inj}$ , the radiative efficiency,  $\eta_r$ , and the light extraction efficiency,  $\eta_e$ . Since  $\eta_r$  and  $\eta_{inj}$  mostly depend on the material growth and device configuration, the photon coupling and loss mechanisms are governed by the light extraction efficiency. As illustrated in Fig. 5.7, the external quantum efficiency of the PC edge emitters fabricated with a twin-guide structure can be expressed as:

$$\eta_{ex,IG} = \eta_e \eta_r \eta_i = \eta_o \eta_{wg} \eta_{ac} \eta_{pc} \eta_{vc} \eta_l \eta_r \eta_{inj}, \quad (1)$$

where

$\eta_l$  accounts for the radiation loss from QD active region to surrounding air;

$\eta_{vc}$  is the vertical coupling efficiency of QD active region to the lower guiding layer;

$\eta_{pc}$  is the coupling efficiency of PC cavity modes to PC modes in waveguide;

$\eta_{ac}$  represents the anti-crossing coupling between PC modes and index-guided modes;

$\eta_{wg}$  represents the propagation loss in the waveguide defined by  $\exp(-\alpha L)$  where  $\alpha$  is the scattering and propagation loss coefficient, and L is the length of the waveguide; and

$\eta_o$  is the output-coupling efficiency at the waveguide facet,  $\eta_o = 1 - R$ , where R is the reflectance at the semiconductor-air interface.

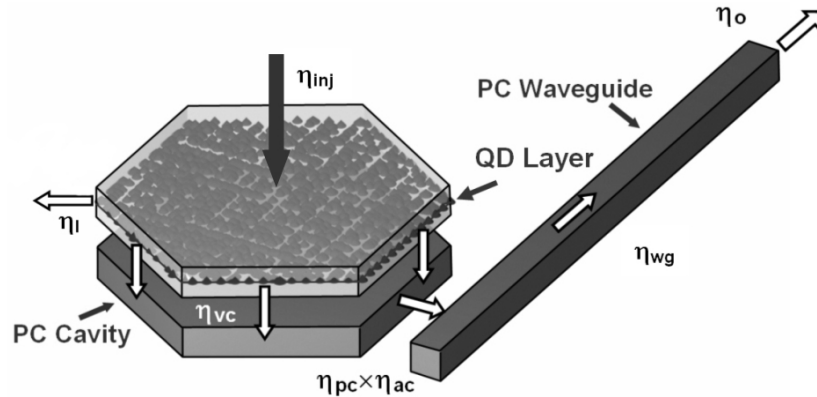


**Fig. 5.7** Illustration of the carrier injection, recombination and the photon extraction processes and their characteristic efficiencies in PC light emitting diodes fabricated with a twin-guide.

A 3% coupling efficiency between cavity modes and waveguide modes is extracted from the measured light-current characteristics of the PC LED with an active region diameter of  $40\mu\text{m}$  transversely coupled to a  $150\mu\text{m}$  long, 3-missing-defect PC waveguide.

The coupling via “anti-crossing” mechanism has been observed for microcavities coupled to W3 waveguides. We have observed similar behavior for W5 and wider waveguides. Cavity coupled transmission spectra for a W5 waveguide is shown in Fig. 5.8.

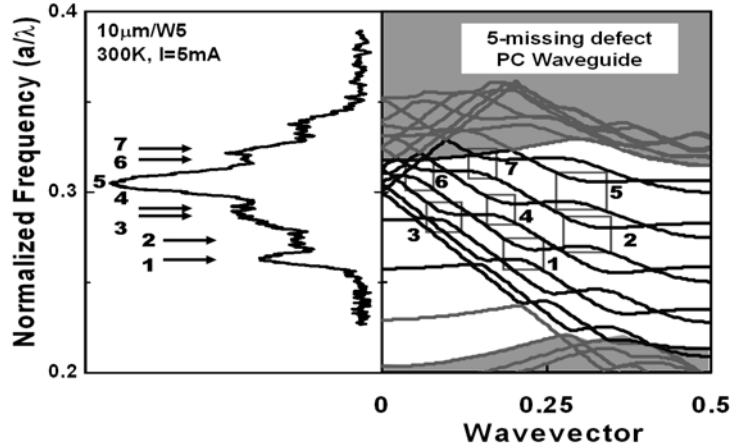


**Fig. 5.8** The emission peaks of a  $10\mu\text{m}$  device compared with the positions of the anti-crossing mini-gaps in the dispersion relation of a 5-missing-defect waveguide, indicated by arrows and rectangles, respectively.

## VI. Photonic Crystal Defect Waveguide Coupled Quantum Dot Photodiode

### Summary

We have investigated the characteristics of an  $\text{In}_{0.4}\text{Ga}_{0.6}\text{As}$  self-organized quantum dot resonant cavity photodiode. The QD epitaxy and the design of the two-dimensional PC cavity were tailored for  $1.3\mu\text{m}$  wavelength operation. The input excitation to the photodiode is provided with an in-plane defect waveguide designed with the same PC similar to the one described in Section 5. The measured spectral photocurrent characteristics reflect the mode coupling between the waveguide and detector and the modal properties of the PC-based waveguide. The characteristics are also dependent of cavity size. The enhancement and narrowing ( $\sim 10\text{nm}$ ) of the photoresponse at  $\lambda\sim 1.3\mu\text{m}$  is explained with a model involving the circulating fields in the cavity. A spectral dip, of  $\sim 10\text{nm}$  width, also observed at  $1.3\mu\text{m}$  is possibly due to the anti-crossing mechanism, uniquely present in PC waveguides.

### Device Design and Fabrication

Light from the input PC waveguide is guided into the 2D PC cavity placed below the detector mesa. This cavity can trap photons and increase their probability of being absorbed in the QD layers of the detector by vertical mode leakage, as shown in Fig. 6.1. The incorporation of the PC resonant cavity effectively eliminates the need for a long absorption length necessary in conventional waveguide photodetectors. The demonstrated

device with the QD absorption region reduces the detector size ten-fold when compared to waveguide photodiodes. The device heterostructure is grown by MBE on  $n^+$  GaAs substrate. Due to the relatively large separation between the four identical QD layers in the active region ( $\sim 30\text{nm}$ ) the coupling between subsequent layers is negligible. The calculated vertical fundamental mode profiles in both the waveguide region and the cavity region are shown in Fig. 6.1.

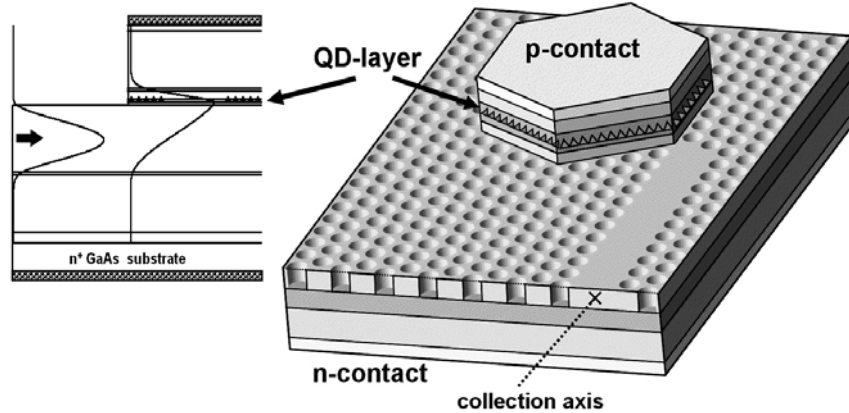


**Fig. 6.1** calculated vertical fundamental mode profiles in both the waveguide region and the cavity region(left) and the device schematic (right).

Device fabrication begins with Pd/Zn/Pd/Au metal deposition for the top p-ohmic contact, followed by the self-aligned mesa formation, using a combination of RIE and wet etching, to eliminate the QD absorber outside the contact region. The PC with a 2D triangular lattice of air-holes is fabricated with the help of electron beam lithography and chemically assisted ion beam etch (CAIBE), with silicon dioxide ( $\text{Si}_x\text{O}_y$ ) serving as the etch mask. The sample is next covered with a  $1\text{-}\mu\text{m}$  thick layer of  $\text{Si}_x\text{O}_y$  for surface passivation. Via-holes are opened in this layer and the interconnect metallization is formed. Finally, the n-ohmic contact is deposited on the backside of the substrate with Ni/Ge/Au/Ti/Au alloyed metallization.

The PC with a triangular lattice of air holes is designed with an effective index  $n_{\text{eff}}=3.35$  for the vertical fundamental mode at  $1.3\ \mu\text{m}$ . In order to scale the position of mid- PBG to  $\sim 1.3\ \mu\text{m}$ , the desired lattice constant is  $a=340\text{nm}$  and the diameter of air holes is  $d_h=220\text{nm}$ . We have fabricated devices of various sizes, with top ohmic contact diameters of 6, 10, 50, and  $100\ \mu\text{m}$ . These devices are coupled to PC waveguides with widths corresponding to 3, 5, 7, and 9 missing defects. The coupling is designed, as shown in Fig. 6.2, such that the cavity resonances are not perturbed considerably. SEMs in Fig. 6.2 reveal that the etched air-holes are about  $800\ \text{nm}$  in depth and have a slight slope on their side walls. It is worth noting that although the waveguide layer is not completely penetrated by the air holes ( $\sim 350\text{nm}$  unetched), the incident light that propagates in the unetched region of the heterostructure that forms the waveguide diverges very rapidly due to the tightly focused spot at the entrance of the waveguide. This results in negligible spurious photocurrent. The non-ideal side-wall profile can contribute to downward photon scattering, or vertical loss. However, we believe that since the cladding layer is relatively thick, such loss should not be significant.

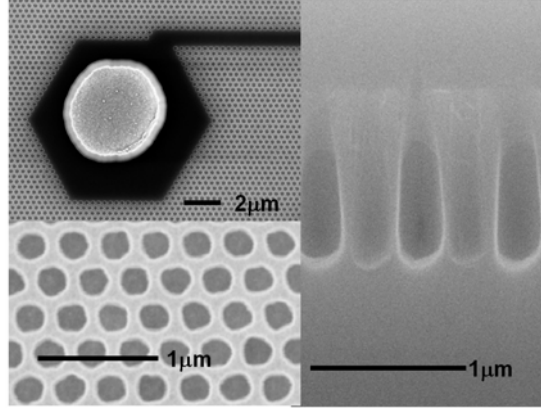


**Fig. 6.2** Scanning electron micrographs of fabricated device showing completed photodiode with input guide and planar and cross-sectional views of the air holes of the 2D photonic crystal. The latter was designed with  $n_{\text{eff}}=3.35$ , the lattice constant,  $a=340\text{nm}$ , diameter of air holes,  $d_h=220\text{nm}$ , and etch depth of  $800\text{nm}$ .

### Device Characterization

Device characterization is performed at room temperature in the wavelength range of  $1.1\text{-}1.4\mu\text{m}$ , using a Coherent RegA optical parametric amplifier (OPA) system (which is tuned to generate a relatively broad-band spectrum), a monochromator with spectral resolution  $\sim 3\text{nm}$ , and a microscope objective with a  $0.40$  numerical aperture (NA) that focuses the light into the PC waveguide cleaved edge. The power of incident light is measured before it enters the monochromator. To estimate the actual power coupled into the QD absorbing layer, the following must be noted. The maximum transmission of the monochromator is  $85\%$ ; the numerical apertures of the focusing objective and the PC waveguide are comparable,  $0.40$  and  $\sim 0.59$ , respectively. The focused spot size of the objective is  $\sim 8\mu\text{m}$  in diameter due to Gaussian beam distortion from the laser. The area of waveguide cross-section is  $2.6\mu\text{m}^2$  for a W9 waveguide, transmittance at the waveguide facet  $70\%$ , and propagation loss coefficient of a PC waveguide is  $\sim 50\text{cm}^{-1}$ , which translates to  $47.2\%$  efficiency for a  $150\mu\text{m}$  long waveguide. Vertical coupling efficiency in a twin-guide scheme is  $\sim 33\%$ . As a result, the fraction of power coupled to the absorber layer is only  $0.48\%$  of the incident power. The power of a monochromatic input is estimated from the spectrum area ratio of the wavelength with a  $3\text{nm}$  linewidth to the total area of the laser output spectrum and is  $\sim 1.5\%$  of the total incident power. The photon-carrier conversion efficiency therefore is  $\sim 0.1\%$  at  $\lambda=1.2\mu\text{m}$  and  $\sim 0.025\%$  at  $\lambda=1.3\mu\text{m}$ , disregarding QD absorption coefficient and other photon and carrier loss mechanisms. Although it is often believed that the quantum efficiency of a waveguide-coupled photodetector is limited by the coupling efficiency of the external excitation to the waveguide, this problem can be alleviated to a large extent when devices such as emitters, waveguides, and detectors are monolithically integrated on the same chip.

Figure 6.3 shows the spectral response of measured photocurrent at reverse bias of  $9\text{V}$  for (a) a  $100\mu\text{m}$  device, i.e.  $r\cong 50\mu\text{m}$ , and (b) a  $50\mu\text{m}$  device, i.e.  $r\cong 25\mu\text{m}$ . The spectral features in Fig. 6.3 (b) for the  $50\mu\text{m}$  device result from a triangular roundtrip resonant path (with its length equal to  $3\sqrt{3}r$ ) in a hexagonal cavity. A relatively narrow

and strong response peak occurs at  $\lambda=1.29\ \mu\text{m}$ , with its full width half maximum (FWHM)  $\sim 10\text{nm}$ . We believe that the photocurrent response at  $\lambda=1.29\ \mu\text{m}$  is enhanced by the defect modes in the PBG ( $1150\text{nm} < \lambda_{\text{PBG}} < 1550\text{nm}$ ).

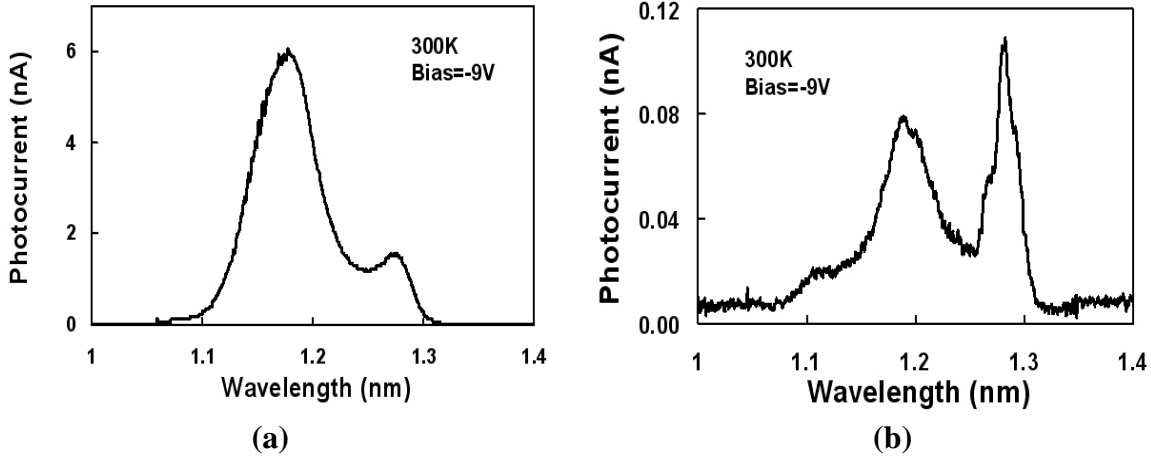


**Fig. 6.3** Measured photocurrent spectra of photodiodes at room temperature and a reverse bias of 9V for devices with (a)  $r=50\ \mu\text{m}$  and (b)  $r=25\ \mu\text{m}$ .

## VII. Theoretical study of Enhanced Spontaneous Emission from InAs Self-Organized Quantum Dots in a 2D GaAs PC Defect Microcavity

### Introduction

Control of the spontaneous emission process has made it possible to achieve high performance optoelectronic devices, such as high efficiency light emitting diodes (LEDs) and nearly thresholdless laser diodes (LDs). Spontaneous emission has been improved by confining electrons in a heterostructure by introduction of QWs and later by QDs, which lead to fully 3D electronic confined systems. With the aid of sub-micron cavities, spontaneous emission can be further enhanced by tuning the optical modes to which the electronic dipole is coupled. It is evident that highly confined electronic and photonic systems can contribute significantly to the enhancement of spontaneous emission.

The initial applications of this newly evolved system can be observed in VCSELs LEDs with lateral oxide confinement, and air-post microcavity LEDs, with QWs and QDs in the active region. However, the approaches employed in these applications are not suitable for integration of emitters, waveguides and detectors. The introduction of PCs, on the other hand, offers a more attractive technique for producing optical microcavities because of their potential for device integration into optical circuits. Optically- and electrically- pumped PC light emitters based on single or multiple defects in a periodic PC have been successfully demonstrated. The PC light emitters reported to date, however, only exploit the localized (defect) mode in the PC microcavity.

For application of surface emitting light sources, the use of the localized mode as the desired cavity mode has some drawbacks. First, the localized mode is an in-plane cavity mode. It can tunnel through the PC laterally, but does not propagate or transport energy to the top of the cavity except by leakage or scattering. Second, both the PBG and the frequency of the localized mode are extremely sensitive to the cavity parameters, such as

the lattice constant and the size of air holes, which cannot be exactly controlled during the fabrication process. Finally, the PBG for a 2D triangular lattice of air holes only affects the transverse electric (TE) or even modes, and has no effect on transverse magnetic (TM) or odd modes. Thus, half of the emission energy in the cavity is eventually dissipated as undesired modes. To overcome these shortcomings, the guided mode, as opposed to the localized mode, is the desired dominant output. The guided modes vertically propagate and carry energy to the top of the cavity. They are less selective to the cavity parameters and are also polarization-insensitive. Therefore, we have chosen a cavity with a length much larger than that of the radius, which, depending on the cavity geometry can support a certain number of guided modes.

The semiconductor confined structures such as strained or unstrained QWs and self-organized QDs serve as the embedded light source inside microcavities. Therefore, to properly describe the characteristics of the spontaneous emission in the PC light emitters, it is essential to consider the confined electronic system, as well as the confined photonic system. QDs possess better optical and electronic properties than QWs due to their atom-like density of states. Although self-organized QDs suffer from the inhomogeneous broadening of the spontaneous emission resulting from the size variation of the dots, the issue becomes less significant in the optical microcavity since only a few dots are enclosed inside the cavity.

We have theoretically investigated the spontaneous emission characteristics of an ensemble of self-organized InAs/GaAs QDs enclosed in the PC microcavity using guided modes as desired cavity modes.

## Calculations

The calculation procedures for computing the spontaneous emission rate from InAs/GaAs self-organized QDs confined in the PC microcavity are divided into three steps. First, the optical modes supported by the cavity are calculated in the frequency domain. Then, the wavefunctions and the electronic states in the QDs are determined from an eight-band  $\mathbf{k}\cdot\mathbf{p}$  formulation, including an appropriate description of the strain tensor in the dots. Finally, the transition matrix element describing the interaction between optical modes and quantum dots is derived and the spontaneous emission rate is calculated using the Fermi golden rule.

The configuration of the microcavity is schematically shown in the inset of Fig.7.1. The lateral confinement of light is provided by multiple reflections from the distributed scatters. The radius of the air hole is chosen to be  $r=0.32a$ , where  $a$  is the lattice constant of the triangular lattice. The finite cavity length imposes a vertical boundary condition on the cavity such that the out-of-plane wave vector,  $k_z=m\pi/L_z$ , where  $m$  is an integer. The cavity length  $L_z$  is chosen to be  $8.75r$ , which determines the interval of the normalized wave vector along the  $z$  direction ( $\Delta k_z = 0.05$ ). The cavity modes are categorized as localized, extended, and guided modes by virtue of their propagation direction and energy concentration.

We use frequency domain analysis to calculate the band structure and the mode distribution in three-dimensional  $k$ -space. A complete mode calculation, including the

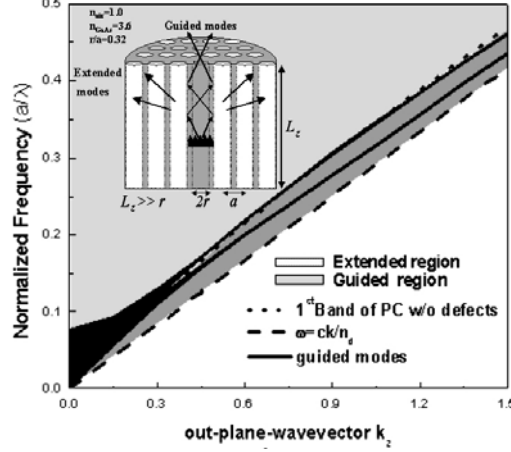


**Fig.7.1.** The out-of-plane band structure of the triangular lattice of air columns with a single defect with inset showing a schematic of the cavity configuration.

localized, guided, and extended modes, allows us to identify the spontaneous emission to each cavity mode. The out-of-plane band structure of the triangular lattice of air holes with a single defect is shown in Fig.7.1 for the first few bands.

As seen in Fig.7.1, the in-plane PBG gradually vanishes as the out-of-plane wave vector,  $k_z$  increases. The localized mode corresponds to the normalized frequency  $a/\lambda=0.238$  at  $k_z=0$ . It is important to note that it is the guided mode in the cavity, and not the localized mode, which will couple with the spontaneous emission from the QDs. The guided modes appear between the region of the first lowest band of the perfect PC and the boundary provided by the refractive index of the defect,  $\omega=ck/n_d$ , where  $n_d$  is the refractive index of the defect. Other cavity modes in the frequency range of interest are the extended modes. The photon density of states in the active region, or the local density of states is expressed as:

$$N_L(r_0, \omega) = \sum_{k_z} \iint_{1stBZ} |A_{n,k}(r_0)|^2 \delta(\omega - \omega_{n,k}) dk_x dk_y \quad (1)$$

where  $A_{n,k}$  are the Bloch functions calculated from the cavity eigenmodes,  $n$  is the band number,  $k$  is the wavevector and the integration extends over the first Brillouin zone. Recent work suggests that for PBG emitters with embedded quantum dots, the position of the atomic dipole affects the photoluminescence spectrum significantly. Thus, an average of the electric field amplitude  $\tilde{A}_{n,k}$  over the area of the active region is a more appropriate representation of the local field experienced by the quantum dots in the entire active region. The calculated local density of states for the photonic crystal microcavity, with lattice constant  $a=0.3\mu\text{m}$ , is plotted in Fig. 7.2. Highly distinctive cavity modes are observed in the frequency range of interest. The peaks mostly originate from the guided modes due to the large electric field intensity in the active region. It is also apparent that the extended modes constitute a uniform background. Since a complete photonic bandgap does not exist in this system, total suppression of the extended modes is impossible. It will be shown later that considerable enhancement of spontaneous emission can be obtained by tuning the guided mode of the microcavity to the peak emission wavelength of the QDs.

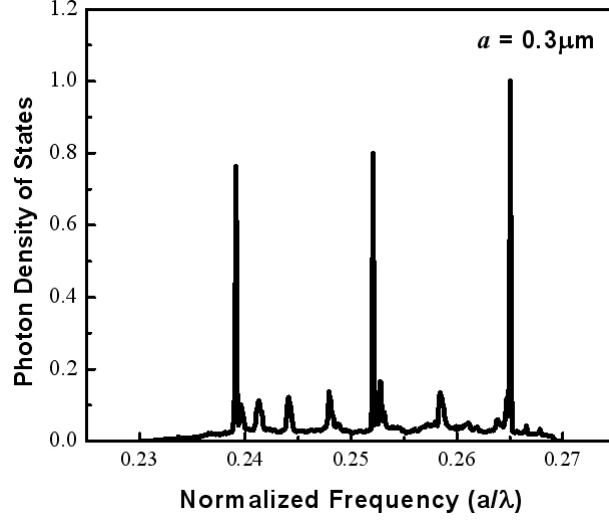


**Fig.7.2.** Calculated local density of states for the photonic crystal microcavity with lattice constant  $a=0.3\mu\text{m}$ . The large peaks correspond to the guided modes and the non-zero background arises from the extended mode linewidths.

Self-assembled  $\text{In}_{1-x}\text{Ga}_x\text{As}$  QDs are formed on GaAs as coherently strained islands when the lattice mismatch exceeds 1.8%. For growth along the [001] direction, these quantum dots are near-pyramidal in shape with a square base in the (001) plane. A typical dot density is  $10^{11} \text{ cm}^{-2}$ . An eight-band  $\mathbf{k}\cdot\mathbf{p}$  formulation, which includes coupling between conduction band and valence band, is used for determining the conduction band and valence band states. The strain tensor in the dots is calculated using the valence force field model of Keating and Martin. The spontaneous emission rate in the cavity can be expressed, using the Fermi golden rule, as:

$$\frac{1}{\tau_{sp}} = \frac{2\pi}{\hbar} \sum_{n,k} \frac{e^2}{m_0^2 \omega_{n,k}} |P_{if}|^2 \frac{1}{\sqrt{2\pi}\sigma} \exp\left(-\frac{(E_c - E_v - \hbar\omega_{n,k})^2}{2\sigma^2}\right) f^e(E_c) f^h(E_v) \quad (2)$$

where  $|P_{if}|^2$  is the transition matrix element to be derived,  $\omega_{n,k}$  is the frequency of the eigenmode in the photonic crystal microcavity,  $f^e, f^h$  are the occupancy of electrons and holes, respectively, and  $E_c$  and  $E_v$  are the energies in the conduction band and valence band. Note that a Gaussian distribution is used to represent the electronic density of states for QDs where the inhomogeneous broadening parameter,  $\sigma$ , results from the size variation of the self-organized QDs. The transition matrix element can be expressed and derived as:

$$|P_{if}|^2 = \left| \langle f | \tilde{A}_{n,k} \bar{\varepsilon} \cdot \bar{P} | i \rangle \right|^2 = \left| \tilde{A}_{n,k}^x | \varepsilon \cdot P |_{env}^x + \tilde{A}_{n,k}^y | \varepsilon \cdot P |_{env}^y + \tilde{A}_{n,k}^z | \varepsilon \cdot P |_{env}^z \right|^2 P_{cv}^2 \quad (3)$$

where  $\tilde{A}_{n,k}$  is the modified electric field amplitude in the cavity,  $\varepsilon$  is the unit polarization vector,  $P$  is the momentum matrix element for electrons,  $| \varepsilon \cdot P |_{env}$  is the envelope function overlap of the wavefunctions,  $P_{cv} = \langle p_x | P_x | s \rangle = \langle p_y | P_y | s \rangle = \langle p_z | P_z | s \rangle$ , and  $2P_{cv}^2/m_0$  is around 20 meV for most semiconductors. It is worth noting that this expression is generally true for QDs in any microcavity and it is also valid for multiple inter-band transitions. It may also be noted that the eigenmode in the cavity is usually normalized such that the

integration of its energy density over space equals unity. To calculate the spontaneous emission rate for each cavity mode, the electrical field amplitude,  $A_{n,k}$  is correspondingly scaled to its total energy,  $\cong \omega_{n,k}$ .

## Results and Conclusions

The spontaneous emission peak is found to be at a photon energy of 1.04eV for a 80Å high, 160Å wide, InAs QD. Assuming that only the ground state transition is dominant in the dots, isotropic effective masses and parabolic dispersion emission relations are valid at the conduction and valence band edges. The carrier injection is chosen such that each dot has two electrons occupying the ground state. We compute the spontaneous emission rate for the InAs QDs placed inside the GaAs PC microcavities and compare this with that in the homogenous medium without a cavity. The mode volume  $V_m$  of a 3D fundamental mode is estimated to be  $5\lambda^3$ , which gives the Purcell factor of  $F_p=15$ . It suggests that the Purcell factor can predict the enhanced spontaneous emission rate for an ideal system where only a single or a few dots are embedded in the microcavity, i.e.,  $\lambda_e=\lambda_c$  and  $\Delta\lambda_e \ll \Delta\lambda_c$ . Otherwise, the enhancement of the spontaneous emission can deteriorate very quickly when the QD emission linewidth becomes much broader than the cavity linewidth, as in the case of high density or multiple layers of self-organized QDs enclosed in the microcavity. The Purcell factor as a function of emission linewidth is shown in Fig. 7.3.

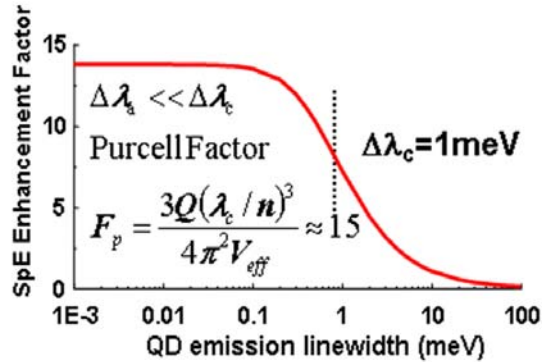


**Fig. 7.3** Calculated spontaneous emission enhancement factor as a function of the emission linewidth.

## VIII. Theoretical Calculations of Defect Modes in a Slab Photonic Crystal for Applications in Photonic Crystal Circuits

### Summary

The work focused on single site impurity modes in photonic crystal slabs. The theory of single site impurity modes was addressed and numerical results for the PC slab between perfectly conducting plates were obtained. An effective mass theory, similar to that used in semi-conductor physics, was worked out from a Wannier function representation.

We have shown that the waveguide modes of the free standing slab could be approximated by those of the PC slab between two perfectly conducting plates. This work was a prelude our work that involves the discussion of the modes bound to and localized about a single site impurity in the PC slab.

### Single Site Impurity

We have studied the theory of a single site impurity in a photonic crystal slab. The photonic crystal slab is a free standing slab of thickness  $d$  containing a hexagonal lattice array (with lattice constant  $a$ ) of cylindrical holes. The holes are of radii  $R$  and contain media of dielectric constant  $\varepsilon_b$ . In the slab, outside the cylindrical holes, the dielectric constant is  $\varepsilon_a$ . The photonic crystal slab is surrounded by media of dielectric constant  $\varepsilon_0$ . A single site impurity is formed by replacing the media of  $\varepsilon_b$  in one of the cylindrical holes with media of dielectric constant  $\varepsilon_c$ .

The electric field,  $\vec{E}(\vec{x})$ , of the single site impurity problem is from Maxwell's equations described by

$$-\nabla^2 \vec{E} + \nabla(\nabla \cdot \vec{E}) - \varepsilon(\vec{x}) \frac{\omega^2}{c^2} \vec{E} = \delta\varepsilon(\vec{x}) \vec{E} \quad (1)$$

Here the dielectric constant of the photonic crystal,  $\varepsilon(\vec{x})$ , is periodic in the plane of the slab.

The impurity media is described by  $\delta\varepsilon(\vec{x}) = \varepsilon_c$  inside the impurity cylinder with

$\delta\varepsilon(\vec{x}) = 0$  otherwise. The fields associated with the impurity can be expanded in the photonic crystal slab modes so that

$$\vec{E}(\vec{x}) = \sum_{\alpha} \int \frac{d^2 k}{(2\pi)^2} b_{\alpha}(\vec{k}_{\parallel}) \vec{E}_{\alpha}^{(0)}(\vec{k}_{\parallel}, \vec{x}) \quad (2)$$

where  $\vec{E}_{\alpha}^{(0)}(\vec{k}_{\parallel}, \vec{x}) = \exp(i\vec{k}_{\parallel} \cdot \vec{x}) \sum_{\vec{G}} \sum_{i=1}^3 a_{i,\alpha}(\vec{k}_{\parallel} + \vec{G}_{\parallel}) \hat{x}_i \exp(i\vec{G} \cdot \vec{x})$

is a mode of the photonic crystal slab (i.e., for  $\delta\varepsilon(\vec{x}) = 0$  everywhere in Eq.(1)) labeled by the band index  $\alpha$  and the wavevector component in the plane of the slab  $\vec{k}_{\parallel}$ , and  $\vec{G}_{\parallel}$  is a reciprocal lattice vector of the hexagonal lattice. Substituting into Eq. (1) gives an eigenvalue problem for the expansion coefficients  $b_{\alpha}(\vec{k}_{\parallel})$

$$\frac{1}{\varepsilon_c} b_{\alpha}(\vec{k}_{\parallel}) = d \frac{\omega^2}{c^2} \frac{1}{\omega_{\alpha}^2(\vec{k}_{\parallel})} \sum_{\vec{G}_{\parallel}, \vec{G}'_{\parallel}} \sum_{\alpha'} \int \frac{d^2 k'_{\parallel}}{(2\pi)^2} \quad (3)$$

$$f(\vec{k}_{\parallel} - \vec{k}'_{\parallel} + \vec{G}_{\parallel} - \vec{G}'_{\parallel}) \left[ \sum_{i=1}^3 a_{i,\alpha}^*(\vec{k}_{\parallel} + \vec{G}_{\parallel}) a_{i,\alpha'}(\vec{k}'_{\parallel} + \vec{G}'_{\parallel}) \right] b_{\alpha'}(\vec{k}'_{\parallel}) \quad (4)$$

Here  $f(\vec{q}_{\parallel}) = \pi R^2 2J_1(\vec{q}_{\parallel} R) / \vec{q}_{\parallel} R$  for  $J_1$  a Bessel function if  $q \neq 0$ ,  $f(0) = \pi R^2$ , and  $\omega_{\alpha}(\vec{k}_{\parallel})$  is the frequency of the  $\vec{E}_{\alpha}^{(0)}(\vec{k}_{\parallel}, \vec{x})$  mode of the photonic crystal slab in the absence of an impurity.

To solve Eq. (3) the frequency of the impurity mode,  $\omega$ , is specified and the eigenvalue problem is solved for the eigenvalue,  $1/\varepsilon_c$ , and the eigenvector,  $\mathbf{b}_\alpha(\vec{k}_\parallel)$ . This gives the dielectric constant of the impurity material needed to support an impurity mode with frequency  $\omega$  and determines the wavefunction of the impurity state.

### **Related Photonic Crystal Work**

The theory of intrinsic localized modes (ILMs) in nonlinear photonic crystal waveguides and circuits has been discussed. Approximate solutions for both even- and odd-parity ILM modes have been reviewed as well as a discussion given of some of the optical bistability properties of photonic crystal circuits. Much of the work has been done by mapping the difference equations of nonlinear photonic crystal circuits onto those of vibrational and magnetic systems that have already been studied in the content of ILM solutions. Results from some other theoretical approaches have also been discussed. Prominent amongst these are numerical solutions of the difference equations and we should also mention some recent work on variational treatments applied to similar difference equations. In addition, some brief discussion is given of the optical bistability properties of the difference equations for Kerr nonlinear media. Optical bistability is the second important phenomenon generally associated with Kerr media. Besides being an interesting property of photonic crystal circuits, it should be a property of the difference equations used to develop the theory of ILMs. The optical bistability properties of the solutions of the set of difference equations are found to be similar to those observed in layered optical media.

Both numerical simulation and analytical studies have been made on vibrational and spin systems to determine the characteristic dynamics of ILMs. The work on photonic crystal waveguides and circuits, however, has mainly been limited to analytical approximations on systems with waveguide channels formed from cylinders having small cross-sectional areas. Both stationary and propagating ILMs in the PC systems have been treated subject to these limitations.

While the theory of photonic crystal waveguides and circuits is simple and gives a quick indication of the types of phenomena which are associated with ILMs in PC circuits, the theory needs to be extended to consider channels formed from cylinders with general cross-sectional areas. Some progress has been made toward this end in the so-called coupled resonator optical waveguide mode theory. In addition, numerical simulation studies are needed to fill out the results of the analytical treatments. Some of these can be obtained from the existing simulations, made on spin and vibrational systems containing ILMs, by taking advantage of the mappings that exist between the difference equations of these systems and the difference equations of the photonic crystal waveguides and circuits. This is currently in progress. While the presentation has been for waveguides in 2D PCs, a tight-binding formulation for propagating modes along waveguides in 3D PC is possible. In three dimensions the difference equation is no longer valid as the dielectric properties of the photonic crystal vary with  $z$  as well as  $x_i$ . However, if the dielectric constants of the sites forming the waveguide channel in a three-dimensional PC are chosen correctly, electromagnetic modes bound to the individual channel sites can tunnel from channel site to channel site to create a waveguide mode which propagates along the waveguide. This type of tunneling between impurities is

observed in semiconductor physics where at high enough donor or acceptor impurity concentrations impurity bands are observed in the semiconductor band gap due to electron tunneling between impurities. These are often described in a tight-binding formulation. A difference in the case of PC is that in PCs one can align the channel sites to form a line (waveguide) along which a propagating mode will appear.

**7. Technology Transfer/Initiative:**

None

**8. Report of Inventions:**

None

**9. Scientific Personnel (Honors/Awards/Degrees Received):**

Graduate Student Research Assistant: J. Topolancik

P. Bhattacharya received the International Quantum Devices Award in 2003. He also received the Nick Holonyak, Jr. Award in 2002 from the Optical Society of America.

**10. Publications and Conference Presentations**

1. "Photonic Crystal Circuits: Localized Modes and Waveguide Couplers", Arthur R. McGurn, *Physical Review B*, **65**, 2002.
2. "Electrically Injected Photonic Crystal Microcavity Light Sources", P. Bhattacharya, J. Sabarinathan, W-D. Zhou, P-C. Yu, and A. McGurn, *IEEE Circuits and Devices*, **19**, 25, 2003.
3. "Band Structure, Density of States, and Modes of Photonic Crystal Slabs", A.R. McGurn, P. Bhattacharya, J. Sabarinathan, W-D. Zhou, and P-C. Yu, submitted to *Physica*, April 2002.
4. "An Electrically Injected InAs/GaAs Quantum Dot Photonic Crystal Microcavity Light Emitting Diode", J. Sabarinathan, P. Bhattacharya, P-C. Yu, S. Krishna, J. C., and D.G. Steel, *Applied Physics Letters*, **81**, 3876, 2002.
5. "Intrinsic Localized Modes in Photonic Crystal Circuits", A.R. McGurn, *Chaos*, **13**, 754, 2003.
6. "Fluid Detection with Photonic Crystal-Based Multichannel Waveguides", J. Topolancik, P. Bhattacharya, J. Sabarinathan, and P-C. Yu, *Applied Physics Letters*, **82**, 1143, 2003.
7. "Enhanced Spontaneous Emission from InAs/GaAs Self-Organized Quantum Dots in a GaAs Photonic Crystal Based Microcavity", Peichen Yu, Pallab Bhattacharya, and Jui-ching Cheng, *Journ. of Appl. Phys.*, **93**, 6173, 2003.

8. "Photonic Crystal Slabs", A.R. McGurn, P. Bhattacharya, J. Sabarinathan, W-D. Zhou, and P-C. Yu, *Physica B*, **338**, 178, 2003, and accepted in conference proceeding of *Sixth International Conference on the Electrical Transport and Optical Properties of Inhomogeneous Media*.
9. "Electrically Injected Photonic Crystal Edge Emitting Quantum Dot Light Source", J. Topolancik, S. Pradhan, P-C. Yu, S. Ghosh, and P. Bhattacharya submitted to *IEEE Photonic Technology Letters*, **16**, 960, 2004.
10. "Characteristics of a Photonic Crystal Defect Waveguide Coupled Quantum Dot Photodiode", P-C. Yu, J. Topolancik, and P. Bhattacharya, submitted to *IEEE J. Quantum Electronics*.
11. "Mode Coupling Characteristics and Efficiency of Quantum Dot Electrically-Injected Photonic Crystal Waveguide-Coupled Light Emitting Diodes", P.C. Yu, J. Topolancik and P. Bhattacharya, submitted to *Journal of Quantum Electronics*, April 2004.
12. "Electrically Injected 1.55 $\mu$ m InP-based Photonic Crystal Microcavity Light Source", Jayshri Sabarinathan, Pallab Bhattacharya, Weidong Zhou, Pei-Chen Yu, S. Mogg, and M. Hammar, Indium Phosphide and Related Materials Conference (IPRM), 425, 2002.
13. "Photonic Crystal Slabs", A.R. McGurn, International Workshop on Photonic and Electromagnetic Crystal Structures, Los Angeles, CA, October 2002.
14. "Photonic Crystal Circuits: Localized Modes and Waveguide Couplers", A.R. McGurn, International Workshop on Photonic and Electromagnetic Crystal Structures, Los Angeles, CA, October 2002.
15. "Intrinsic Localized Modes in Nonlinear Photonic Crystal Circuits", A.R. McGurn, 2002 Materials Research Society Fall Meeting, Boston, MA, December 2002.
16. "Intrinsic Localized Modes in Photonic Crystal Circuits", A.R. McGurn, 27<sup>th</sup> Workshop: Intrinsic Localized Modes and Discrete Breathers in Nonlinear Lattices, Erice-Sicily, Italy, July 2003.
17. "Electrically Injected Photonic Crystal Edge Emitting Quantum Dot Light Source", J. Topolancik, IEEE/LEOS Semiconductor Laser Workshop, Baltimore, MD, June 2003.
18. "Two Dimensional Photonic Crystal Active and Passive Devices", (INVITED), P. Bhattacharya, J. Topolancik, J. Sabarinathan, S. Pradhan, and P-C. Yu, 30<sup>th</sup>

*International Symposium on Compound Semiconductors*, San Diego, CA, August, 2003.

19. “Electrically Injected Photonic Bandgap Microcavity Light Sources”, (INVITED), P. Bhattacharya, W. D. Zhou, J. Sabarinathan, and P-C. Yu, *IEEE Lasers and Electro-Optics Society (LEOS) Annual Meeting*, San Diego, November 2001.
20. “High-Speed Quantum Dots and 2\_D Quantum Dot Photonic Crystal Light Sources”, (INVITED), P. Bhattacharya, *International Symposium on Quantum Dots and Photonic Crystals*, Tokyo, Japan, November 2003.